JACS
JOURNAL OF THE AMERICAN CHEMICAL SOCIETY

ARTICLE

pubs.acs.org/JACS

Covalency in the 4f Shell of *tris*-Cyclopentadienyl Ytterbium ($YbCp_3$)—A Spectroscopic Evaluation

Robert G. Denning,*[,†] Jeffrey Harmer,[‡] Jennifer C. Green,[†] and Mark Irwin[†]

[†]Department of Chemistry and [‡]Center for Advanced Electron Spin Resonance, Department of Chemistry, University of Oxford, South Parks Road, Oxford OX1 3QR, United Kingdom

Supporting Information

ABSTRACT: Evidence is presented of significant covalency in the ytterbium 4f shell of tris-cyclopentadienyl ytterbium ($YbCp_3$) in its electronic ground state, that can be represented by the superposition of an ionic configuration Yb(III):$4f^{13}(Cp_3)$ and a charge-transfer configuration Yb(II):$4f^{14}(Cp_3)^{-1}$. The relative weights of these configurations were determined from (i) the difference in their 4f photoionization cross sections, (ii) the accumulation of spin-density centered on the ^{13}C atoms of the Cp ring, as measured by a pulsed EPR (HYSCORE) experiment, (iii) the reduction in the spin-density in the 4f shell, manifest in the ^{171}Yb hyperfine interaction, and (iv) the principal values of the *g*-tensor, obtained from the EPR spectrum of a frozen glass solution at 5.4 K. Each of these methods finds that the spin density attributable to the charge transfer configuration is in the range 12−17%. The presence of configuration interaction (CI) also accounts for the highly anomalous energies, intensities, and vibronic structure in the "f−f" region of the optical spectrum, as well as the strict adherence of the magnetic susceptibility to the Curie law in the range 30−300 K.

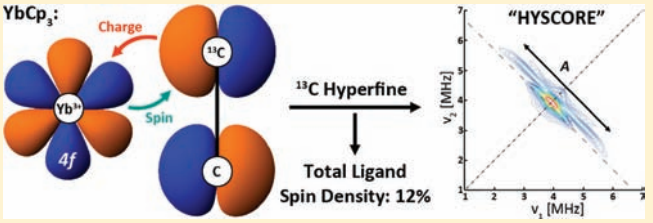

1. INTRODUCTION

The high electropositivity of the lanthanides, together with the contracted and screened character of the 4f valence shell, is often taken to imply that, in the ubiquitous III oxidation state, covalency is insignificant and the bonding is primarily electrostatic. However, electron-rich and strongly basic ligands, such as cyclopentadienyl (Cp) and bis(trimethylsilyl)amido anions, form volatile compounds, soluble in nonpolar noncoordinating solvents, in which ligand-to-metal charge-transfer must be substantial. The photoelectron spectroscopy of $CeCp_3$[1] and $LuCp_3$[2] taken together with theoretical work[3] indicates that interactions with the lanthanide 5d shell are the primary source of this covalency.

In the 4f shell any covalency is more difficult to quantify, but it is often taken to be negligible. However, the energy-selective photoelectron spectrum (PES) of $YbCp_3$ strongly suggests that the ground state can be described as an admixture of the Yb(III):$4f^{13}L$ and Yb(II):$4f^{14}L^{-1}$ configurations, where L refers to the ligand molecular orbitals (MO) collectively.[2] With the exception of $EuCp_3$ (for which $E_{1/2} = -1.54$ V, relative to the SHE, in THF solution), $YbCp_3$ has a less negative reduction potential ($E_{1/2} = -1.92$ V) than other $LnCp_3$,[4] so configurations involving charge-transfer from electron-rich ligands to the ytterbium atom should be most apparent in this compound. There is, for example, strong magnetic and spectroscopic evidence in compounds of the type $Cp^*_2Yb(bipy)$ that both the $|f^{14}(bipy)\rangle$ and $|f^{13}(bipy)^-\rangle$ configurations are represented in the ground state.[5−7]

In this paper we present experimental evidence from (i) our previous PES data,[2] (ii) new EPR measurements, and (iii) existing electronic spectroscopic studies[8,9] that allows a semi-quantitative determination of the extent of this class of configuration interaction (CI) in $YbCp_3$. The strikingly anomalous electronic spectrum of $YbCp_3$ in solution,[9] and excellent quality spectra in the solid state at low temperatures,[8] are long-standing observations that have, for the most part, remained uninterpreted. In what follows, we demonstrate that the high symmetry of this compound, together with the presence of Kramers degeneracy, makes the description of the main features of its electronic structure, and the interpretation of its physical properties, relatively straightforward.

As an aside, we note that routine computational methods have not proved satisfactory in addressing this problem. For example, two different DFT codes give values for the spin density on the Yb atom of 39 and 57%. Apart from their mutual inconsistency, when set against our experimental results, both methods seriously overestimate the extent of spin transfer onto the ligands. Despite this inadequacy, DFT calculations have proved useful in establishing certain characteristics of the electronic structure.

2. METHODS

2.1. Crystal Growth. $YbCp_3$ was prepared as described previously.[2] A concentrated toluene solution in a Schlenk tube, under argon, was

Received: October 3, 2011
Published: November 04, 2011

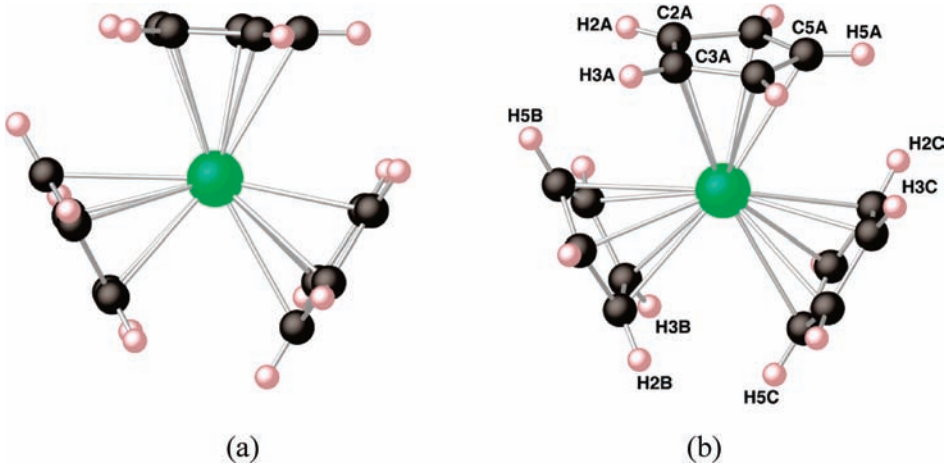

Figure 1. Structure of $YbCp_3$ at 105 K, (a) emphasizing the nominal C_3 axis, and (b) showing nonbonded inter-ring interactions.

placed in a −40 °C freezer. After 2 days, green blocklike crystals of $YbCp_3$, suitable for single-crystal X-ray diffraction, had formed.

2.2. X-ray Crystallography. Data were collected using an Enraf-Nonius Kappa-CCD diffractometer and a 95 mm CCD area detector with a graphite-monochromated molybdenum Kα source (λ = 0.71073 Å). Crystals were selected under Paratone-N oil, mounted on MiTeGen loops, and slowly cooled to 105 K, using an open flow N_2 cooling device, at a rate of 1 K per minute.[10] Data were processed using the DENZO-SMN package, including unit cell parameter refinement and interframe scaling (using SCALEPACK within DENZO-SMN).[11] Structures were subsequently solved using direct methods, and refined on F^2 ($R1$ = 0.0194, $wR2$ = 0.0447) using the SHELXL 97−2 package.[12,13]

2.3. Electron Paramagnetic Resonance. X-band CW EPR experiments were performed on a Bruker BioSpin GmbH EMX spectrometer equipped with a high sensitivity Bruker probe−head, and pulse EPR experiments were carried out at X-band on a Bruker E680 spectrometer using a 4 mm dielectric ring resonator (EN 4118X-MD4). Both instruments were equipped with Oxford Instruments helium-flow cryostats. All pulse data were recorded at 9.7512 GHz and 3.75 K. The EPR spectrum was recorded by integrating the FID created with an 800 ns microwave (mw) pulse. Hyperfine sublevel correlation (HYSCORE)[14,15] experiments employed the pulse sequence $\pi/2-\tau-\pi/2-t_1-\pi-t_2-\pi/2-\tau-$echo using the following parameters: mw pulses of lengths $t_{\pi/2}$ = t_π = 16 ns, starting times of 96 ns for t_1 and t_2, and time increments Δt = 16 ns (data matrix 400 × 400) and τ = 114 ns. An eight-step phase cycle was used to remove unwanted echoes. The HYSCORE data were processed with MATLAB 7.0 (The MathWorks, Inc.). The time traces were baseline corrected with an exponential, apodized with a Gaussian window, and zero filled. After a two-dimensional Fourier transformation, absolute-value spectra were calculated. The CW EPR and HYSCORE spectra were simulated with the program EasySpin.[16]

2.4. Raman Spectroscopy. A solid sample was flame-sealed in a Pyrex capillary under dinitrogen. The spectrum was recorded on a Dilor Labram 300 spectrometer, using 20 mW He−Ne laser excitation, at 632.8 nm. To minimize photodecomposition, this laser power was attenuated by a factor of 100. The counting time was 120 s. The spectrometer was calibrated before each measurement by reference to the 520.7 nm line of a Si wafer.

2.5. Computation. Density functional calculations were carried out using the Amsterdam Density Functional program suite ADF 2010.2.[17−19] Scalar relativistic corrections were included via the ZORA method for all calculations.[20−23] The generalized gradient approximation was employed, using the local density approximation of Vosko, Wilk, and Nusair[24] together with the nonlocal exchange correction by Becke[25,26] and nonlocal correlation corrections by Perdew.[27] TZP basis sets were used with triple-ζ accuracy sets of Slater type orbitals and polarization functions added to the main group atoms. The cores of the atoms were frozen up to 1s for C and 4d for Yb. Default conditions were used for the optimizations and frequency calculations. Calculations were also performed using the Gaussian program suite.[28] The latter employed the B3LYP functional[24,29−31] and SDD basis sets with a Stuttgart−Bonn relativistic effective core potential for Yb.

3. RESULTS

3.1. Structure and Geometry of $YbCp_3$. The single crystal X-ray structure of $YbCp_3$ was first reported[32] in 1987. One of the Cp rings was found to be disordered, so the structure was refined using D_{5h} symmetry and fixed bond lengths in that ring. The structure has now been redetermined at 105 K; it is effectively unchanged but is more precise, and there is no evidence of disorder.

The molecular symmetry is close to C_{3h} (Figure 1a), with the planes of the Cp rings being almost exactly parallel to the pseudo-3-fold axis; they are, however, tilted about axes parallel to C_3 so that the Yb−C5 distances are ∼0.1 Å longer than Yb−C2 and Yb−C3. A space-filling model implies that this arises from steric interactions between the rings and that the ring orientations may be constrained by the interlocking of the C5/H5 atoms in the notional C_{3h} plane, with C2/H2 and C3/H3 on adjacent rings (Figure 1b).

Selected bond lengths and angles are listed in the Supporting Information. The distances from the Yb atom to the centroids of the rings are 2.359(2), 2.343(2), and 2.357(2) Å. The Yb atom is displaced by 0.055 Å along the normal to the plane formed by the ring centroids, which is substantially larger than the offset of 0.010 Å from the centroid of centroids within that plane. The centroid−Yb−centroid angles are 119.40(7)°, 120.47(7)°, and 119.96(7)°.

The shortest intermolecular contact is Yb(1)−C4C(2) = 4.042(4) Å (cf. packing diagram in Figure S1 of the Supporting Information). However, there is no significant difference between the Yb(1)−C4C(1) and Yb(1)−C1C(1) distances (cf. table in the Supporting Information), which are locally related by

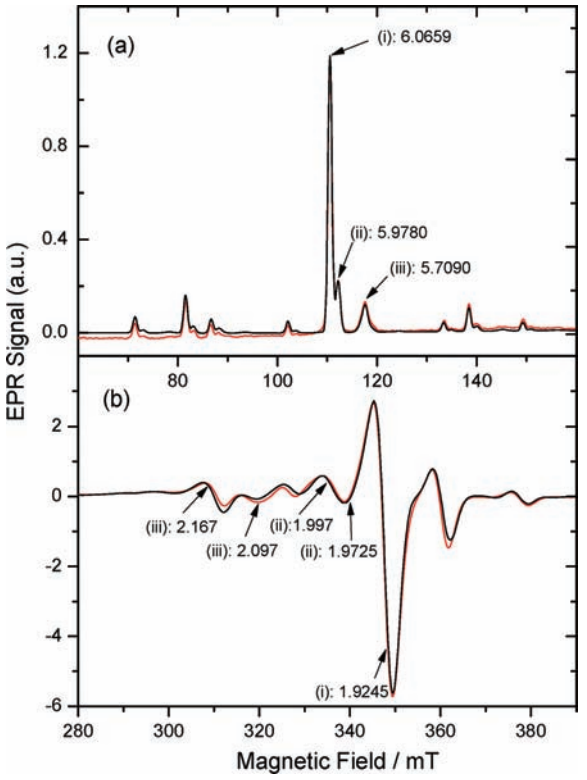

Figure 2. X-band CW EPR spectrum of $YbCp_3$ at 5.25 K (red), and simulated (black).

the nominal C_{3h} plane, so intermolecular interactions do not appear to be electronically significant.

Equivalent distances in the pyrazine-bridged adduct $Cp_3Yb(\mu$-pyrazine)$YbCp_3$ are longer, at 2.43(1), 2.38(1), and 2.42(1) Å, and the average of the N−Yb−Cp(centroid) angles is 98.5°.[33] A similar flattened tetrahedral geometry is found in the triphenylphosphine oxide adduct, in which the O−Yb−Cp(centroid) angles average 100°,[34] as well as in $LnCp_3$ ammonia[35] and THF[36] adducts, where these angles are ∼98.5°. In these adducts, the Yb offset from the plane of the ring centroids is typically 0.35 Å.

3.2. Electron Paramagnetic Resonance. *3.2.1. CW X-Band EPR in Frozen Glass Solution.* The 9.386 GHz spectrum of a ∼1 mM frozen glass solution of $YbCp_3$ in an equimolar mixture of benzene, toluene, and heptane at 5.25 K is shown Figure 2.

The features between 110 mT and 120 mT in Figure 2a, marked (i), (ii), and (iii), imply that three species are present. Component (i), whose spectrum can be fitted to an axial spin Hamiltonian, accounts for 77% of the intensity. Components (ii) and (iii) constitute 15.7% and 7.7% of the intensity, respectively, with a *g*-tensor that appears to be orthorhombic in both cases. The satellites, seen clearly in Figure 2a, are due to the ^{171}Yb ($I = {}^1/_2$) and ^{173}Yb ($I = {}^5/_2$) hyperfine interactions. These nuclei have natural abundances of 14.4% and 16.2%, respectively.

The differences between the principal values of the *g*-tensor for all three species are small, implying that variations in the electronic and geometrical structure are also small. The axially symmetric *g*-tensor of component (i) is consistent with the C_{3h} symmetry expected in the noncoordinating solvent. The lower symmetry of species (ii) and (iii) is, we believe, due to the

Table 1. Spin-Hamiltonian Parameters for $YbCp_3$ in a Frozen Glass at 5.25 K

	⊥	∥
g_{ii}	1.9245	6.0659
^{173}Yb, A_{ii}/MHz	354	1322
^{171}Yb, A_{ii}/MHz	1287	−4805

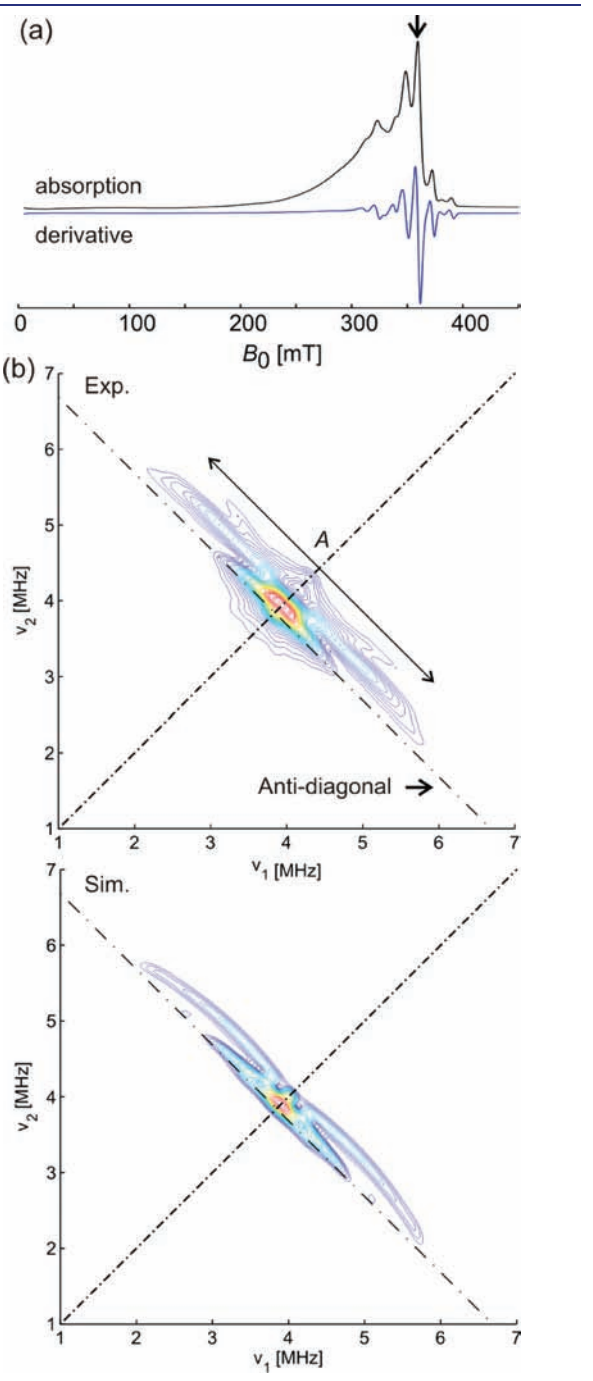

Figure 3. (a) FID-detected EPR spectrum of $YbCp_3$ (black) and its numerical first derivative (blue). (b) HYSCORE recorded near $g_\perp$ (see arrow in part a) showing the ^{13}C region: experiment (top) and simulation (bottom) using A_s = 0.4 and A_p = 1.6 MHz.

trapping of different relative ring orientations within the glass. A simulated spectrum using the spin-Hamiltonian parameters in Table S8 of the Supporting Information is shown in black in Figure 2. Agreement with experiment is good in the low-field region and also above 335 mT, but it is less good between 315 and 335 mT. In the latter region, there are too many unconstrained variables associated with components (ii) and (iii) for further refinement to be useful. Only the properties at the C_{3h} site (i), for which the parameters (Table 1) are well-defined, merit further discussion.

3.2.2. Pulsed X-Band EPR. Figure 3a shows the absorption spectrum at 9.75 GHz, detected by integration of the free-induction decay of the magnetization following a selective 800 ns microwave pulse. The numerical derivative of the absorption spectrum is comparable to that in Figure 2. However, due to the short T_2 time of molecules with $g_{\|}$ aligned parallel to the static magnetic field, the resonances near 110 mT are not detected (the spectrometer dead-time is ~100 ns).

HYSCORE measurements[14] were made at 359 mT and at 300 mT, at which fields the ^{13}C nuclear resonance frequencies are 3.844 and 3.212 MHz, respectively. At 359 mT a group of molecules, oriented with their C_3 axes within a small solid angle that is close to perpendicular to the static field, are in resonance with the microwave field.

HYSCORE spectra correlate a nuclear frequency in the α electron spin manifold with a nuclear frequency in the β electron spin manifold. In the weak coupling case ($2|\nu_{^{13}C}| < |A|$) cross-peaks occur in the (+,+) quadrant, as is the case in Figure 3b. The hyperfine couplings are approximately given by the splitting around $|\nu_{^{13}C}|$ as indicated, and anisotropy in the hyperfine matrix is proportional to the maximum shift of the cross-peaks behind the antidiagonal. The simulation shown is the sum of five ^{13}C hyperfine couplings from a Cp ring and is discussed in section 4.5.

3.3. Vibrational Spectroscopy. The frequencies, in the ground electronic state, of those modes that give rise to vibronic structure in the electronic absorption spectrum are summarized in Table 2. They come from several sources, including the Raman spectrum measured in this work, and can be assigned by using the predictions of a DFT calculation, along with data from a survey of Cp compounds.[37] They remain constant to within ~5 cm^{-1} across a series of $LnCp_3$ (Ln = La, Pr, Nd, Sm, Gd, Dy, Tm).[38] The full data set is in Table S2 and Figure S2 of the Supporting Information.

3.4. Electronic Spectroscopy. *3.4.1. Data Sources.* The absorption and emission spectra of $YbCp_3$ in benzene solution, together with those of several adducts, were reported in 1983 by Schlesener and Ellis.[9] In 1967 the absorption spectrum of solid $YbCp_3$, sublimed onto a quartz window, was measured by Pappalardo and Jørgensen[8] at nominal temperatures of 4.2, 77, and 298 K. Neither publication contains any significant analysis of the spectral details. Both groups used the legendary Cary 14 spectrophotometer, and both sets of diagrams appear to have been reproduced photographically from the instrument charts. Where necessary, we have used a graphics editor to separate overlaid traces in the original diagrams and also to remove a weak sharp band in the solution spectra at 985 nm attributed[9] to a decomposition product. Edited traces were then digitized automatically (Digitizeit: www.digitizeit.de).

Table 2. Selected Vibrational Frequencies

expt (cm^{-1})	C_{3h}	D_{5h} mode no.[37]	D_{5h} irrep	description
112	E′			Cp−Yb−Cp in plane bend
147	A′			sym C−Yb−C asym stretch
196	E′			asym C−Yb−C asym stretch
215	A″			sym ring tilt about axis in plane
241	A′			Yb−Cp sym stretch
255	E′			Yb−Cp asym stretch
619	E′	14	E_2''	CCC out of plane deformation
846	E′	12	E_2'	CCC in plane bend
1065	E′	11	E_2'	C−H in plane bend
1356	E′	10	E_2'	C−C in plane stretch

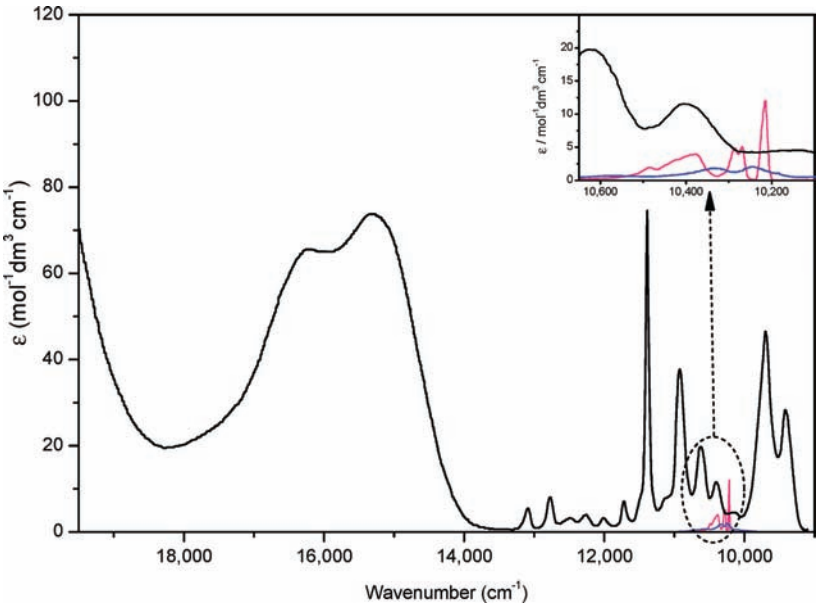

Figure 4. Spectrum of a 5.5 mM solution of $YbCp_3$ in benzene−path-length 1 cm, after Schlesener et al.[9] Inset: the spectra of $YbCp_3$ (black), $Yb(dpa)_3 \cdot 13H_2O$ at 15 K (red), and KY_3F_{10} at 298 K (blue).

Table 3. Integrated Intensities in the $^2F_{7/2} \rightarrow {}^2F_{5/2}$ Region

compd	oscillator strength/10^{-6}
$YbCp_3$ (9,000−13,500 cm^{-1})	182
$Yb(dpa)_3 \cdot 13H_2O$, at 15 K[39]	5.1
KY_3F_{10} at 298 K[40]	3.1
Yb^{3+}(aqueous) at 298 K[41]	3.3

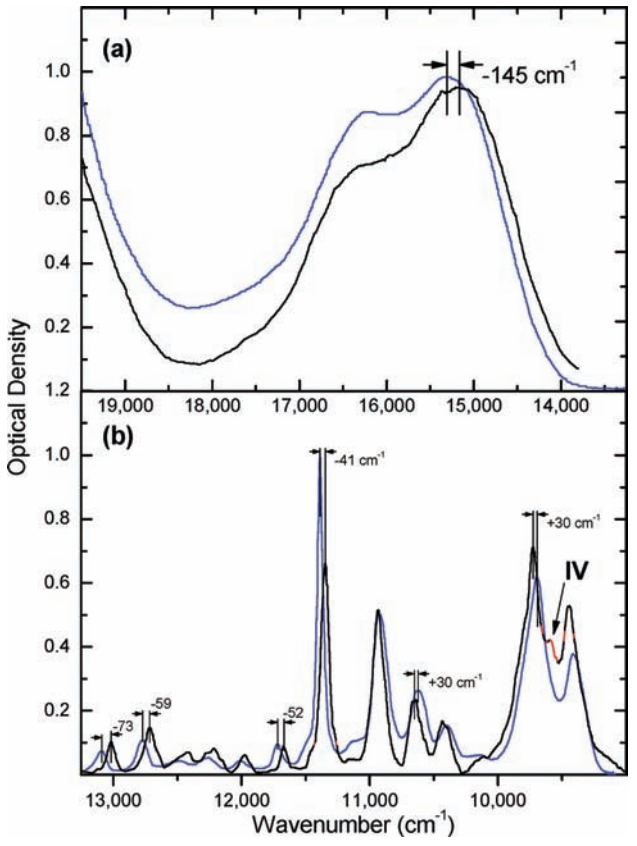

Figure 5. Spectrum of $YbCp_3$ at 298 K in benzene solution, from Schlesener et al.[9] (blue), and in the solid state, from Pappalardo and Jørgensen[8] (black).

The solid sample was mounted in an evacuated glass cell in an immersion cryostat, but its temperature was not measured.[8] The paper states that low noise spectra in the near-infrared were taken in short time intervals, immediately after the liquid He level fell below the light path. The long time constants needed to acquire high resolution low-noise spectra in this region (where the responsivity of the PbS detector is poor) suggest that the data were acquired in short spectral segments, during each of which the vacuum-mounted sample would be susceptible to warming. Anomalies and discontinuities in the spectra appear to indicate that several such segments have been concatenated. A strongly sloping baseline in the low temperature spectra of the solid between 500 and 650 nm is absent at room temperature, implying that scattering increases sharply at shorter wavelengths, possibly due to microscopic fracturing of the "as deposited" glassy film on cooling. A subjective baseline correction was therefore applied in order to establish comparability with the room temperature spectrum.

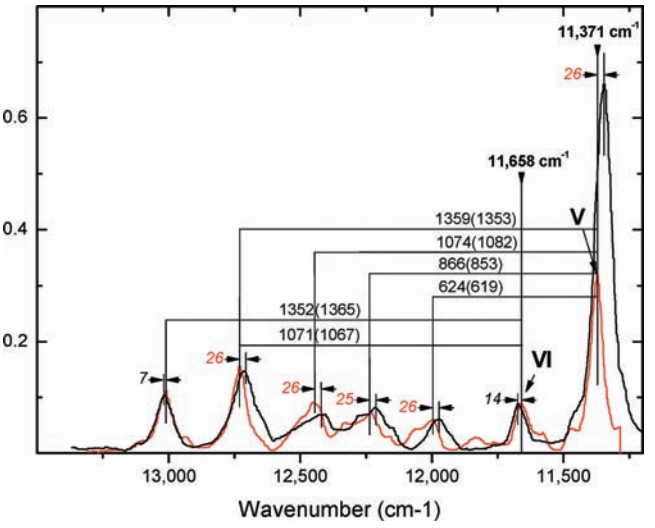

Figure 6. Spectrum at 4.2 K (red) and 298 K (black). Shifts to lower energy with increasing temperature are shown in red, and those to higher energy are in black.

3.4.2. General Characteristics. The spectrum of $YbCp_3$ in benzene solution is shown in Figure 4 together with the spectra of two conventional Yb^{3+} compounds with known absorption cross sections, $Yb(dpa)_3 \cdot 13H_2O$ (dpa = 2,6-pyridinedicarboxylate) at 15 K (shown in red)[39] and Yb^{3+} doped into a crystal of KY_3F_{10} at room temperature (in blue).[40] The structure in the range 9000−13,500 cm^{-1}, a region in which the $^2F_{7/2} \rightarrow {}^2F_{5/2}$ transitions of Yb^{3+} would normally be expected and which in the reference compounds spans <400 cm^{-1}, is highly anomalous and indicates the presence of strong vibronic coupling. The oscillator strength in this region is between 20 to 50 times greater than that in conventional Yb^{3+} complexes (Table 3).

3.4.3. Comparison between the Solid State and Benzene Solution. The thickness of the solid films was not measured,[8] so the optical density in Figure 5 has been chosen subjectively to match that in solution. The geometry and the electronic structure of $YbCp_3$ in the two phases are evidently almost identical. However, sections of the spectrum experience small, distinctive shifts between the two media. For example, the group of sharp bands below 11,200 cm^{-1} shift up by ∼30 cm^{-1} in the solid state relative to their positions in solution, whereas those in the range 11,200−13,500 cm^{-1} shift down by ∼50 cm^{-1} and the broad band above 13,500 cm^{-1} shifts down by ∼145 cm^{-1}. The first group is therefore assigned to one electronic state, while those in the second group are attributable to one or more higher energy electronic states.

3.4.4. From 11,200 to 13,250 cm^{-1}. The spectrum of the solid in this range at room temperature (black) and (nominally) at 4.2 K (red) is shown in Figure 6. Five bands shift down in energy by ∼25 cm^{-1} when the temperature is raised from 4.2 to 298 K, whereas those at 11,658 and 13,000 cm^{-1} show smaller shifts to higher energy, suggesting that they are associated with a different electronic state.

The intervals measured graphically in Figure 6 assume the presence of two electronic origins at 11,371 and 11,658 cm^{-1}. Values in parentheses are calculated from the original authors annotations.[8] Similar intervals have been reported by Amberger et al.[42] in the adducts $Cp_3Yb \cdot L$, where L = methyltetrahydrofuran or cyanocyclohexane, and they found that they matched the

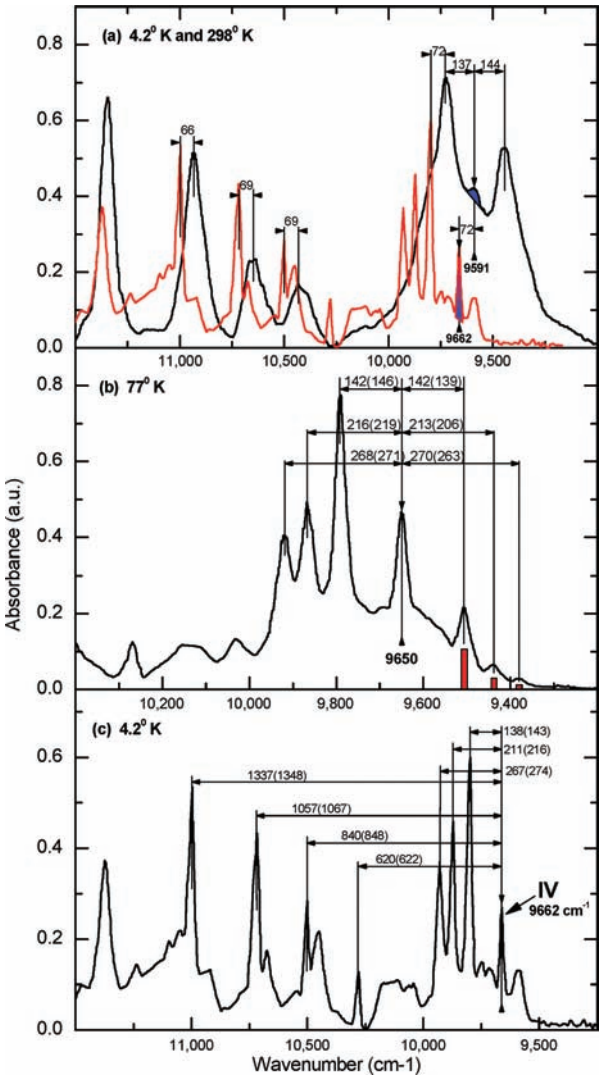

Figure 7. Spectrum from 9,000 to 11,400 cm^{-1} at (a) 4.2 K (red) and 298 K (black), (b) 77 K, and (c) 4.2 K.

frequencies of Raman active modes in these adducts and also in pristine Cp_3Nd and Cp_3Dy. Their assignments were reinforced by deuterium isotope shifts between the spectra of $Cp_3Yb\cdot$Me-THF and $(Cp\text{-}d_5)_3Yb\cdot THF\text{-}d_8$ at 90 K.[42] The Raman spectrum of $YbCp_3$ has not been reported, but our measurements show bands at 1356, 1065, 846, and 619 cm^{-1} (section 3.3 and Table 2) that match these intervals. Because the feature at 13,000 cm^{-1} is 1629 cm^{-1} above the origin at 11,371 cm^{-1}—an interval that has no counterpart among the internal modes of the Cp ligands[37]—it is assigned to a sideband on the origin at 11,658 cm^{-1}, with which it shares a distinctive temperature shift (cf. Figure 6).

3.4.5. From 9,000 to 11,200 cm^{-1}. Figure 7a compares the spectra in this region at nominal temperatures of 4.2 and 298 K. The prominent hot band intensity near 9500 cm^{-1} suggests that the sharp band at 9662 cm^{-1} (at 4.2 K) is an origin. This is confirmed in the 77 K spectrum (Figure 7b), in which the origin shifts down by 12 cm^{-1} and the three prominent sidebands at 142, 216, and 268 cm^{-1} are replicated on its low energy side by hot bands with similar intervals, and with relative intensities that match those calculated (red bars) for a temperature of 120 K.

Table 4. $YbCp_3$ Band Energies and Oscillator Strengths[a]

spectral region	energy/cm^{-1}	temp/K (nom)	$f/10^{-6}$
	$YbCp_3$ Soln (Gaussian Fit)		
	13,500−18,000	298	730
	9,000−13,500	298	180
	Origin Bands (Solid)		
IV	9,661	4.2	2.4
V	11,371	4.2	7.0
	11,345	298	20 (26)[b]
VI	11,658	4.2	1.9
	11,672	298	1.9
VII	15,151	4.2	6.4
VIII	23,530	4.2	~10^4
IX	26,060	4.2	~10^4
	$YbCp_3\cdot$Pyrrolidine, Soln		
IV	9,802	298	64
V	10,788	298	34
VI	10,822	298	
	Vibronics on Origin (Solid)		
IV	9,250−11,200	4.2	61
		298	150 (130)[b]
V and VI	11,500−13,260	4.2	20
		298	27 (16)[b]
VII	14,225−19,510	4.2	480
	13,350−17,930	298	660 (800)[b]
	$YbCp_3\cdot$Pyrrolidine, Soln		
VII	13,925−18,280	298	1100

[a] Note: Oscillator strengths ±25% due to band overlap and estimated path length. [b] Solution value.

In Figure 7c the strong sharp features in the 4.2 K spectrum exhibit the same vibronic intervals as those in Figure 6. All the structures below 11,200 cm^{-1} undergo a uniform ~70 cm^{-1} red shift at room temperature (Figure 7a), confirming that it is built on the origin at 9662 cm^{-1}.

In the axial ligand field of $YbCp_3$, the $^2F_{7/2}$ free ion state splits into four Kramers doublets, so the origin at 9662 cm^{-1}, which is the first component of $^2F_{5/2}$, corresponds to a transition to the fourth Kramers doublet above the ground state and is labeled IV, while those at 11,371 and 11,658 cm^{-1} are labeled V and VI, respectively.

There are several other points of interest in Figure 7.

(i) A weak hot band at 9590 cm^{-1} in Figure 7c indicates difficulty with the control of the sample temperature (section 3.4.1).

(ii) At 298 K origin IV (filled blue in Figure 7a) shifts to the red by the same 72 cm^{-1} increment as the vibronic structure built on it. Low frequency modes at 138, 211, and 267 cm^{-1}, and particularly the first of these, make a prominent contribution to the vibronic intensity, but these are not discernible as sidebands on origins V and VI. The intense and characteristic pair of bands near 9445 and 9725 cm^{-1}, that contribute the bulk of the intensity in the near IR, are due to the hot and cold vibronic features respectively associated with the ~140 cm^{-1} mode.

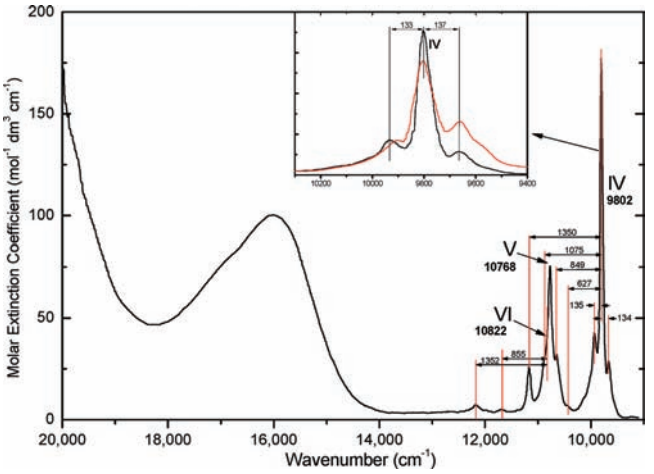

Figure 8. Absorption spectrum of $YbCp_3 \cdot$pyrrolidine adduct in benzene. Inset: absorption (black) and emission (red) in the region of origin IV.

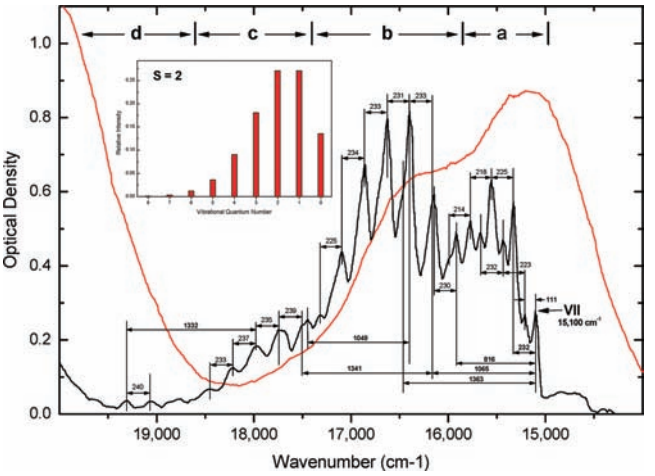

Figure 9. Spectrum of solid $YbCp_3$ at 4.2 K (black) and at 298 K (red). Inset: Progression with Huang−Rhys parameter $S = 2$.

Modes at 144, 231, and 243 cm^{-1} appear in the equivalent region in the methyl-THF adduct.[42]

(iii) The oscillator strength of origin IV at 4.2 K is ∼25 times weaker than the vibronic intensity built on it (Table 4), whereas in the Me-THF adduct the origins are much more intense than the associated vibronic structure.[42] The implication is that origin IV in $YbCp_3$ is forbidden in C_{3h} or D_{3h} symmetry but becomes allowed in the C_{3v} symmetry of $YbCp_3 \cdot L$ adducts.

(iv) This is confirmed by the solution spectra of these adducts.[9] When L = pyrrolidine, origin IV at 9802 cm^{-1} is much more intense than the 135 cm^{-1} pair of hot and cold vibronic sidebands (Figure 8), with the latter being the more intense. In emission,[9] origin IV is found at 9800 cm^{-1}, but the higher energy of the two ∼135 cm^{-1} sidebands is, as expected, the less intense "hot" component (Figure 8, inset). The other sharp features in this figure display the same vibronic intervals as those in $YbCp_3$.

(v) Finally, the weak feature in Figure 7a at 9591 cm^{-1} attributed to origin IV in solid $YbCp_3$ is absent in benzene solution (Figure 5b), despite the otherwise close similarity of the spectra. In the solid, the Yb atom is displaced 5.5 pm away from the plane formed by the centroid of Cp rings (section 3.1), and the symmetry approximates to C_{3v}. The implication is that origin IV is forbidden in the C_{3h} symmetry of the solution species.

3.4.6. From 14,000 to 20,000 cm^{-1}. Figure 9 shows the 4.2 K and room temperature spectra in the red region. This band was originally assigned to a Cp → Yb charge transfer transition, on the basis of the energies of analogous transitions in several $LnCp_3$.[8] The relatively low resolution does not allow a complete assignment; nevertheless, several features are informative.

(i) A prominent progression in a ∼230 cm^{-1} mode can be assigned to the symmetric M−Cp stretch. This occurs in each of the spectral sections a, b, c, and d in the figure, and exhibits an intensity pattern compatible with a Huang−Rhys parameter $S \approx 2$ (Figure 9, inset)—a value that implies an increase in the M−Cp bond length in the excited state of ∼20 pm.

(ii) The intensity in sections b and c decreases at room temperature, but there is a large increase both in section a and also below 15,000 cm^{-1}. Both changes are to be expected if the vibronic intensity is derived from modes with $h\nu \approx kT$, and these changes are reminiscent of the temperature dependence around origin IV in Figure 7a. A substantial increase in intensity integrated over the whole of the band indicates that a vibronic mechanism dominates; however, further analysis is not worthwhile because of the subjective baseline correction applied to the 4.2 K spectrum.

(iii) If the sharp band at 15,100 cm^{-1} is taken as origin VII, then the vibronic intensity at intervals of 111 cm^{-1} and 232 cm^{-1} is comparable to that found on origin IV. The ∼230 cm^{-1} progressions based on VII and on these sidebands can account for all the features in section a up to 15,850 cm^{-1}. The weakness of origin VII can again be attributed to an intrinsically electric-dipole forbidden transition, whose intensity comes from the small distortion from C_{3h} symmetry in the solid state.

(iv) Additional vibronic "false" origins are required to account for the structure in section b, and these appear at intervals of 816, 1065, and 1363 cm^{-1}. They are in reasonable agreement with their analogues in Figure 7c. A progression of up to 5 quanta in the ∼230 cm^{-1} mode can be identified in this region.

(v) Further progressions appear in section c above 17,400 cm^{-1} with a similar intensity pattern to those in section b. Their position suggests that they are built on further quanta of 1049 and 1341 cm^{-1}—similar frequencies to those encountered previously. A weak echo of this structure occurs in section d and could be built on an additional quantum of ∼1332 cm^{-1}.

Comparing Figures 4 and 8, the intensity of the higher energy of the two broad components near 17,000 cm^{-1} in the pyrrolidine adduct, and 16,250 cm^{-1} in $YbCp_3$, is substantially unchanged ($\varepsilon_{max} \sim 55$), while ε_{max} rises substantially from ∼60 to ∼90 in the lower energy component centered at 16,000 and 15,250 cm^{-1}, respectively.[9] This implies that intensity has been added in the vicinity of the pure electronic transition (and the 230 cm^{-1} progression built on it) in the C_{3v} pyrrolidine adduct,

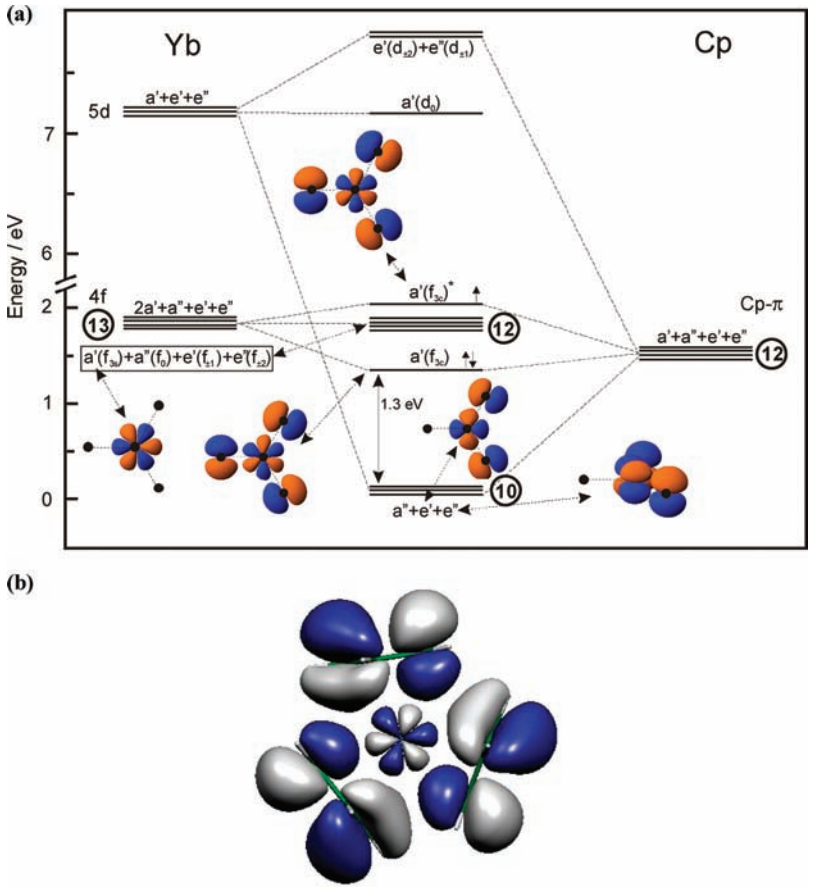

Figure 10. (a) Schematic MO diagram for $YbCp_3$, showing the occupation numbers, symmetry, and nodal structure of selected orbitals. The $a'(f_{3c})$, $a'(f_{3c})^*$, and $a'(f_{3s})$ MOs include 4f orbitals that are functions of cos 3ϕ and sin 3ϕ. Note the break in the energy scale. (b) The vacant $a'(f_{3c})^*$ frontier MO, as given by a DFT calculation.

and it is analogous to the changes near origin IV in Figure 8. Table 4 shows that, relative to the pristine $YbCp_3$, the band area based on origin VII increases by ~35% in the pyrrolidine adduct.

3.4.7. From 14,000 to 29,500 cm^{-1}. A thinner film of solid $YbCp_3$ at 78 K (Figure 4 of ref 8) shows two broad intense bands with maxima at 23,530 and 26,060 cm^{-1}, corresponding to excited states we label VIII and IX. The sloping baseline and unknown thickness make their intensity uncertain, but by reference to the band at ~16,000 cm^{-1}, whose intensity is known in solution, both bands have $\varepsilon_{max} \sim 1800$ cm^{-1} mol^{-1} dm^3 and a fwhm of ~3000 cm^{-1}, with an implied oscillator strength of ~0.01 and a transition dipole length of ~20 pm. The vertical energies of these transitions, relative to the maximum of the 230 cm^{-1} progression on origin VII near 15,500 cm^{-1} (Figure 9), are 1.0 and 1.30 eV, respectively.

3.5. Density Functional Calculations. Density functional calculations were carried out using both a pure density functional and a hybrid method (section 2.5). While conscious of the limitations of these methods for treating highly correlated systems, they have proved useful in estimating the size of the C2p/Yb4f overlap, in determining the coefficients of the ring π-orbitals, and in assigning the vibrational modes.

Both methods indicate delocalization of the spin density away from the Yb atom. The ADF calculation gave the residual spin density on Yb as 39% and the Gaussian calculation as 57%.

4. DISCUSSION

4.1. Preliminaries. *4.1.1. Structure and Symmetry.* $YbCp_3$ is the only tris-cyclopentadienyl lanthanide whose structure is effectively molecular in the solid state—in all other examples there is significant Cp bridging between lanthanide ions. At 105 K the Yb site symmetry is close to C_{3h} (Figure 1a), although the Yb atom is displaced by 5.5 pm above the plane of the centroids of the rings, and intermolecular interactions appear to be negligible (section 3.1). A close resemblance between the electronic absorption spectra in the solid and in benzene solution (Figure 5) confirms that the symmetry is effectively the same in both media; the C_{3h} point group is therefore adopted in the following discussion.

4.1.2. Orbital Symmetries and Energies. Figure 10a is a schematic MO diagram for $YbCp_3$. The relative orbital energies in this figure are approximately correct, but they should not be used to estimate excitation energies. The frontier orbitals of ytterbium are 4f, 5d, and 6p, and those of the Cp ligand are the π-bonding set transforming as e_1'' in D_{5h}. Three of the Cp-$\pi(e_1'')$ components are symmetric with respect to the $YbCp_3$ horizontal plane and form a basis for a′ and e′ MOs in C_{3h}, while the antisymmetric set form bases for a″ and e″. The Yb 5d transform as a', e′, and e″, and the 6p (not shown in the figure) as a″ and e′. However, the net overlap of the cylindrically symmetrical $5d_0(a')$ with the Cp-π (a') MO, which has six nodes in the horizontal plane (Figure 10), is negligible—in D_{3h} they would belong to different irreducible representations. The Yb(5d/6p)−(Cp-π)

interactions therefore lead to a set of filled Cp-centered MOs whose energies have been established both by PES and by density functional theory,[2,3] and which decrease in the order $a' \gg e' \approx e'' \approx a''$, with $YbCp_3$ $(\varepsilon_{a'} - \varepsilon_{e'}) = 1.30$ eV (cf. Figure 10a).

In C_{3h} the 4f orbitals ($f_\phi \equiv f_{\pm 3}$, $f_\delta \equiv f_{\pm 2}$, $f_\pi \equiv f_{\pm 1}$, $f_\sigma \equiv f_0$) transform as follows: $f_\phi - 2a'$, $f_\delta - e''$, $f_\pi - e'$, $f_\sigma - a''$. In a real basis only the cos 3ϕ component of f_ϕ interacts with the a′ HOMO centered on the Cp-rings, while the sin 3ϕ component is effectively orthogonal to it and retains virtually pure 4f character (section S5.2 of the Supporting Information; orbital #28A). The nodal structure of selected MOs is illustrated in Figure 10a. Figure 10b provides a representation of the vacant metal-centered a′ MO generated by the DFT (ADF) code. The remaining f orbitals can interact with the more stable group of Cp-π orbitals, but as a result of their larger energy mismatch, the participation of charge-transfer configurations involving this group should be relatively small; they are shown as degenerate in Figure 10a.

4.1.3. Wave Functions and Overlap. The ADF-DFT calculations use triple-ζ Slater orbitals as bases, yielding a typical 4f-L($2p_\sigma$) overlap integral of 0.019. This is comparable to previous evaluations for lanthanides with oxide and fluoride ligands,[43−47] e.g. the Yb^{3+}(4f)-oxide-$2p_\sigma$ integral has been calculated to be 9.3×10^{-3}.[45] This is small enough to allow the Yb-4f and Cp-π orbitals to be treated as effectively orthogonal. In particular, the overlap density is insignificant in the normalization of the ground state wave function, which can be expressed as the superposition of two Slater determinants, i.e.

$$\Psi_g = c_0\Psi_0 + c_1\Psi_1 = c_0|f^{13}a_1'(L)^2\rangle + c_1|f^{14}a_1'(L)^1\rangle \quad (1)$$

with the latter being derived from the former by charge-transfer from the Cp ring to the Yb^{3+} ion.

Hubbard has pointed out[48] the advantages of using charge-transfer configuration interactions, rather than the familiar molecular orbital method, to describe weak covalent interactions in transition metal complexes. This is primarily due to the incorporation of single-center electron-correlation interactions that can be different in the ionic and charge-transfer configurations. It is also clear that, when considering the Yb-4f−Cp-π interaction, a Heitler−London trial wave function is more appropriate than an LCAO basis. If the extent of the CI is small, we may write the following:

$$c_1 = (\langle\Psi_0|\hat{H}|\Psi_1\rangle - \langle\Psi_0|\hat{H}|\Psi_0\rangle\langle\Psi_0|\Psi_1\rangle)/(\langle\Psi_0|\hat{H}|\Psi_0\rangle - \langle\Psi_1|\hat{H}|\Psi_1\rangle) \quad (2)$$

where $\hat{H}$ is the Hamiltonian operator. In the present case, the denominator in eq 2 can be construed as the energy difference between the configurations after an allowance has been made for all the Yb−Cp bonding interactions, including, for example, those involving the Yb 5d shell but excluding the Yb-4f/Cp-π CI. In what follows we make use of a variety of experimental data to determine c_1 while noting that the energy of the Cp-$\pi \rightarrow$ Yb-4f charge-transfer transition is a function of both the numerator and denominator in eq 2. The magnetic and electronic spectral properties, taken together, do, however, make it possible to quantify not only the intrinsic energy difference of the configurations given by $\langle\Psi_0|\hat{H}|\Psi_0\rangle - \langle\Psi_1|\hat{H}|\Psi_1\rangle$ but also the magnitude of the CI matrix element $\langle\Psi_0|\hat{H}|\Psi_1\rangle$.

4.2. Photoelectron Spectroscopy. The photoionized states are unambiguously attributable to two configurations,[2] i.e., $\Psi_2 = |f^{12}a_1'(L)^2\rangle$ and $\Psi_3 = |f^{13}a_1'(L)^1\rangle$, where Ψ_2 should be taken to include the numerous states associated with this configuration. When $h\nu$ = 240 eV, there are no indirect "shake-up" or "shake-down" excitations in the spectrum of $LuCp_3$, nor is there any evidence for them in $YbCp_3$ at the same energy. In a direct photoionization process, the states collectively described by Ψ_2 are only accessible from Ψ_0 in eq 1, while the Ψ_3 states can be reached either from Ψ_1 by a 4f-electron ionization or from Ψ_0 by a Cp ionization. However, the carbon-2p ionization cross section at $h\nu$ = 240 eV is negligible, so the last of these contributions can be ignored. The intensities arising from the two terms in eq 1 can be then be expressed as follows:

$$I_0 \propto c_0^2|\langle f^{13}a_1'(L)^2|\boldsymbol{\mu}|f^{12}a_1'(L)^2, e^-\rangle|^2$$
$$I_1 \propto c_1^2|\langle f^{14}a_1'(L)^1|\boldsymbol{\mu}|f^{13}a_1'(L)^1, e^-\rangle|^2 \quad (3)$$

where $\boldsymbol{\mu}$ is the electric-dipole moment operator, and the implied proportionalities are identical in both cases. In eq 3 the implicit sum for a one-electron operator gives $I_1/I_0 = 13c_1^2/14c_0^2$. The experimental intensities at $h\nu$ = 240 eV listed by Coreno et al.[2] give $I_1/I_0 = 0.126$, whence $c_1^2 = 0.120$ and $c_1 = 0.346$. Thus, 88% of the density in the ground state can be attributed to the "ionic" Yb^{3+}, $|f^{13}a_1'(L)^2\rangle$ configuration while the Yb^{2+} $|f^{14}a_1'(L)^1\rangle$ "charge-transfer" configuration contributes 12%.

4.3. Valence-Shell Electronic Structure. In this section we construct an electronic structural model, incorporating states derived from the charge-transfer configuration Ψ_1, that is quantitatively compatible with the observed magnetic and electronic spectroscopic properties. An energy level diagram will illustrate how these properties evolve as a function of the extent of the CI.

4.3.1. Bases. Single-particle "hole" functions are convenient. The relevant $YbCp_3$ states are classified in the C_{3h}* double-group (in Bethe's notation).[49] Other charge-transfer hole states involving the deeper lying Cp e′, e″, and a″ MO are of lesser importance and will be ignored for the time being. In C_{3h}* the double-valued irreducible representations occur as one-dimensional complex conjugate pairs, and the free-ion $4f^{13}$ $|jm_j,3^1/_2m_lm_s\rangle$ basis states, abbreviated as $|m_j,m_l^{\pm}\rangle$, together with the ligand $|a'^{\pm}\rangle$ hole states, transform as follows:

Γ_7; $\left|\frac{7}{2},3^+\right\rangle$, $\left|-\frac{5}{2},-3^+\right\rangle$, $\left|-\frac{5}{2},-2^-\right\rangle$, $|a'^+\rangle$

Γ_8; $\left|-\frac{7}{2},-3^-\right\rangle$, $\left|\frac{5}{2},3^-\right\rangle$, $\left|\frac{5}{2},2^+\right\rangle$, $|a'^-\rangle$

Γ_9; $\left|\frac{1}{2},1^-\right\rangle$, $\left|\frac{1}{2},0^+\right\rangle$

Γ_{10}; $\left|-\frac{1}{2},-1^+\right\rangle$, $\left|-\frac{1}{2},0^-\right\rangle$

Γ_{11}; $\left|\frac{3}{2},2^-\right\rangle$, $\left|\frac{3}{2},1^+\right\rangle$

Γ_{12}; $\left|-\frac{3}{2},-2^+\right\rangle$, $\left|-\frac{3}{2},-1^+\right\rangle$

Table 5. Empirical Hamiltonian Parameters and Energy Levels (cm^{-1})

parameter	B_0^2	B_0^4	B_0^6	B_6^6	ζ	ΔE_{M-L}	δ_{CI}	
value	1131	−61	−33	−80	−2760	6100	−3900	
state	Γ_7, Γ_8	Γ_7, Γ_8	Γ_{11}, Γ_{12}	Γ_9, Γ_{10}	Γ_7, Γ_8(IV)	Γ_{11}, Γ_{12}(V)	Γ_9, Γ_{10}(VI)	Γ_7, Γ_8(VII)
calc	0	1,831	2,090	2,184	8,945	11,658	11,836	16,066
expt	0				9,661	11,371	11,658	~15,650

4.3.2. The Hamiltonian. A perturbation Hamiltonian, operating on these bases, can be written as follows:

$$H' = H_{SO} + V_{CF} + H_{int} \quad (4)$$

where $H_{SO} = \zeta_{4f}\,\mathbf{l}\cdot\mathbf{s}$ is the spin−orbit interaction, V_{CF} is the crystal-field (CF) potential experienced by the 4f electrons due to the charge on the Cp rings, together with the anisotropy in the 5d orbital occupancy (section S3 of the Supporting Information), and H_{int} quantifies the Yb−Cp covalent interaction between the $|f^{14}a_1'(L)^1\rangle$ and $|f^{13}a_1'(L)^2\rangle$ configurations, whose energy difference is ΔE_{M-L} (i.e., the denominator in eq 2).

Expansion of a C_{3h} (scalar) potential operating on the 4f shell gives the following:

$$V_{CF} = B_0^2C_0^{(2)} + B_0^4C_0^{(4)} + B_0^6C_0^{(6)} + B_6^6(C_6^{(6)} - C_{-6}^{(6)})$$

where the $C_q^{(k)}$ are irreducible spherical tensor operators and the B_q^k are Wybourne's pseudotensors.[50] The latter are functions of the coordinates of the carbon atoms, on which fractional point charges are presumed to reside, as well as of the average values $\langle r^n\rangle_{4f}$. The carbon coordinates were taken from the crystal structure—idealized to the C_{3h} geometry, while values of $\langle r^n\rangle_{4f}$ that satisfactorily describe the crystal field interaction in Yb^{3+}-doped LaF_3 crystals are given by Morrison and Leavitt.[51] The deficiencies of the point-charge CF model are well-known; nevertheless, the use of empirical values of $\langle r^n\rangle_{4f}$ should provide an effective parametrization of those parts of the Hamiltonian that operate within the "ionic" configuration Ψ_0.[46]

The horizontal plane in C_{3h} ensures that ligand sums within the B_3^4 and B_3^6 pseudotensors vanish. Consequently, V_{CF} has no trigonal components; it is primarily an axial field perturbation; the small hexagonal B_6^6 component will be seen to have little effect.

The ligand-centered a′ MO exhibits a cos 3ϕ angular dependence (Figure 10). The nonzero matrix elements of the CI, H_{int}, can then be parametrized by the following:

$$\delta_{CI} = \langle a'^{\pm}|H_{int}|3^{\pm}\rangle = \langle a'^{\pm}|H_{int}|-3^{\pm}\rangle$$

4.3.3. The Ground State. The concentration of negative charge close to the *xy* plane preferentially stabilizes the hole in the $f_{\pm3}$ orbitals, making the ground state a Γ_7,Γ_8 Kramers doublet whose separation from other states in the manifold can be augmented by its interaction with the $|a'^{\pm}\rangle$ charge-transfer states. Its magnetic properties are readily calculated from the eigenvectors in the Γ_7 (or Γ_8) block.

The spin−orbit interaction is the leading perturbation, so in first order, the ground state approximates to the $^2F_{7/2}$ Yb^{3+} free ion state. The axial field splits this into four doublets with energies in the order $m_J = \pm^7/_2 < \pm^5/_2 < \pm^3/_2 < \pm^1/_2$—the first two of which transform as Γ_7,Γ_8. In the absence of further perturbations, the Γ_7 ground state wave function is $|(^7/_2),3^+\rangle$,

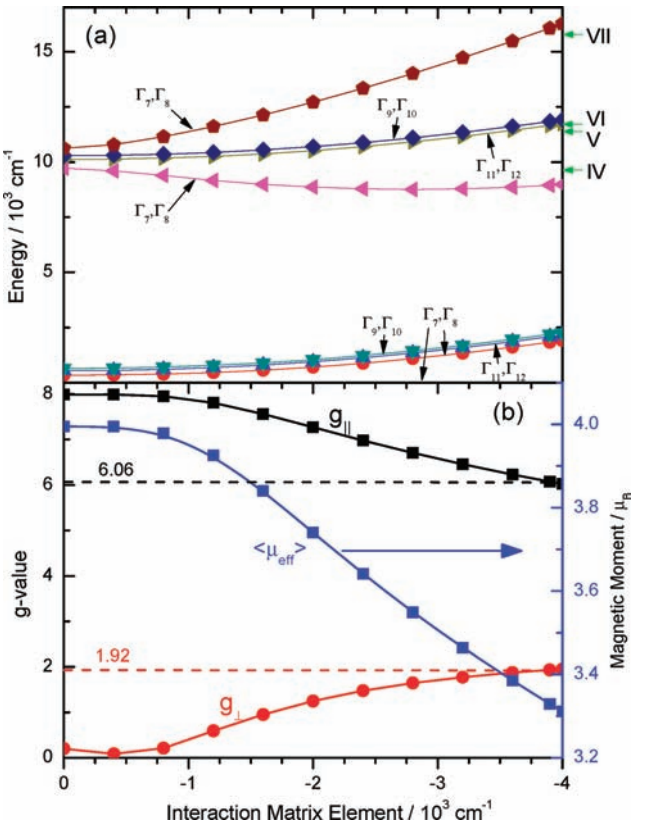

Figure 11. (a) Energy levels and (b) *g*-values and magnetic moment as a function of the CI matrix element.

while that of the first excited state is $(^6/_7)^{1/2}|(-^5/_2),-3^+\rangle+(^1/_7)^{1/2}|(-^5/_2),-2^-\rangle$. These two states are mixed by the B_6^6 component of the potential, but this is too small to alter the ground state properties significantly. Assuming that the ligand hole has isotropic spin-only angular momentum, the magnetic properties of the ground state are then dominated by the relative contributions of the $|(^7/_2),3^+\rangle$ and $|a'^+\rangle$ states, and they should, therefore, be a sensitive indicator of the value of the CI coefficient c_1.

4.3.4. g-Values and Magnetic Moments. For reference, $\zeta_{4f} = -2952\ cm^{-1}$ fits the spectrum of Cs_2NaYbF_6[52] and is used as a trial value. The B_q^k values in Table 5 were evaluated using the literature[51] values $\langle r^2\rangle = 1.74 \times 10^{-21}\ m^2$, $\langle r^4\rangle = 3.94 \times 10^{-41}\ m^4$, and $\langle r^6\rangle = 9.12 \times 10^{-61}\ m^6$, assuming a point charge of $0.2e^-$ on each carbon atom.

The remaining three parameters were chosen to fit the experimental *g*-values as well as the energies of the four excited states that can be identified in the absorption spectrum (*vide infra* and section 3.4.6). The results of this calculation are shown, as a function of δ_{CI}, in Figure 11.

dx.doi.org/10.1021/ja209311g |*J. Am. Chem. Soc.* 2011, 133, 20644–20660

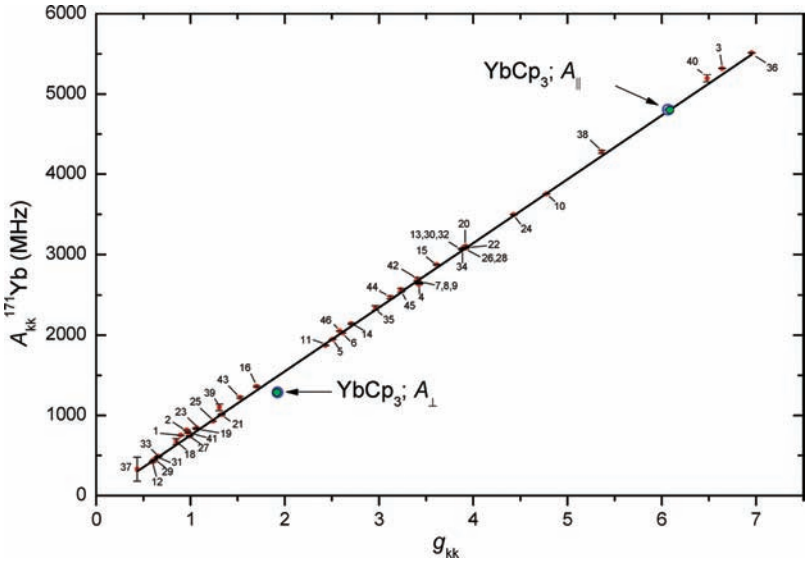

Figure 12. *g*-values and ^{171}Yb hyperfine coupling constants for 29 compounds. For the numbered sources, see section S6 of the Supporting Information. For $YbCp_3$, experimental values are blue circles and simulated values are green dots.

When $\delta_{CI} = 0$, the ground state is that of an ionic f^{13} ion in a strong axial field, and its $|(\pm^7/_2), \pm 3^{\pm}\rangle$ wave function would predict $g_{\|} = 8$ and $g_{\perp} = 0$, although the inclusion of the small B_6^6 perturbation gives $g_{\|} = 7.98$ and $g_{\perp} = 0.20$ (Figure 11b). As δ_{CI} increases, the *g*-values converge toward the EPR values (in glassy solution) of $g_{\|} = 6.059$ and $g_{\perp} = 1.924$, shown by dashed lines in the figure. The parameters of Table 5 with $\delta_{CI} = -3900$ cm^{-1} predict $g_{\|} = 6.071$ and $g_{\perp} = 1.932$, a magnetic moment of 3.33 μ_B, and $c_1^2 = 0.124$.

The experimental susceptibility of the solid, over a wide range of temperature, is accurately described by a moment of 3.53 μ_B.[2] The difference from the EPR solution value may arise from a higher dielectric constant in the solid, which would stabilize the more polar "ionic" limit and reduce the extent of charge transfer. In Figure 11b the magnetic moment (blue) increases as the CI decreases, so the experimental value is consistent with this hypothesis.

In Figure 11a an interaction matrix element that is consistent with the *g*-values in Figure 11b also places the first excited state at >1000 cm^{-1} and thus accounts for the accurate Curie law dependence of the susceptibility between 20 and 300 K.[2]

4.4. The ^{171}Yb Hyperfine Interaction. The dipolar part of this interaction is a linear function of the expectation value $\langle r_i^{-3}\rangle$, where r_i is the electron−nuclear distance. For an electron localized in the 4f orbitals of a free Yb^{3+} ion, $\langle r_i^{-3}\rangle$ is calculated to be 12.85 Bohr^{-3}.[53] If the ground state is derived exclusively from the $^2F_{7/2}$ free ion state, the ratio of the principal values of the dipolar part of the *A* tensor to those of the *g* tensor should be a constant.[54] Figure 12 demonstrates this using 46 sets of ^{171}Yb EPR data from 28 different Yb^{3+}compounds (section S6 of the Supporting Information), most of which are oxides or fluorides with cubic or axial site symmetry and are expected to have the properties of the $4f^{13}$ ion. The slope of this plot gives $A_{kk}/g_{kk} = 796 \pm 2.5$ MHz.

The intercept of -43 ± 3 MHz in Figure 12 is attributable to the isotropic (contact) hyperfine coupling and agrees adequately with the value of -21 ± 17 MHz reported many years ago.[54] The scatter in Figure 12 is due to small second-order contributions from $^2F_{5/2}$ introduced by crystal field perturbations; these can, if required, be treated quantitatively.[55]

In $YbCp_3$ second-order contributions of this kind only arise from the small hexagonal component of the field and are not significant, so the ∼11% reduction in $A_{\perp}/g_{\perp}$ to 712 MHz (assuming that the isotropic coupling is unchanged), which is very clear in Figure 12, cannot be accounted for by V_{CF} operating on the $4f^{13}$ configuration. In the charge-transfer configuration, any spin density centered on the ring carbon atoms, for which Yb−C ∼ 2.65 Å, makes a negligible contribution to $A_{\perp}$ because $r_i^{-3} \approx 0.008$ Bohr^{-3}, which is $\sim 5 \times 10^{-4}$ smaller than that from the 4f density. The spin-only moment of the ligand-centered density does, however, contribute to $g_{\perp}$. The decrease in $A_{\perp}/g_{\perp}$ therefore offers an independent measure of the extent of CI.

At first sight, this argument fails to explain why $A_{||}/g_{||}$ appears to fit the linear relationship in Figure 12. However, the 5d-covalency, implied by DFT calculations and by the PES data, has been ignored. The population in the 5d shell will screen the 4f shell, decreasing $\langle r_i^{-3}\rangle_{4f}$ and thus both $A_{\perp}$ and $A_{||}$. Relativistic Dirac−Fock calculations give $\langle r_i^{-3}\rangle_{4f} = 12.85$ and 12.15 Bohr^{-3} for $j = 7/2$ electrons in Yb^{3+} and Yb^{2+} ions, respectively,[53] demonstrating the effect of a decrease in Z_{eff} in the 4f shell.

We now assume that the value of $\langle r_i^{-3}\rangle_{4f}$ that fits the linear relationship in Figure 12 can be scaled by a factor α in $YbCp_3$ to account for the orbital expansion resulting primarily from the 5d covalency, but we ignore any effect on the isotropic coupling. We then take

$$\mathbf{g} = 2\mu_B\{c_0^2\langle 4f|\mathbf{L} + 2\mathbf{S}|4f\rangle + c_1^2\langle \pi_{Cp}|2\mathbf{S}|\pi_{Cp}\rangle\} \quad (5)$$

Using $\alpha = 0.88$ and $c_1^2 = 0.17$ together with the observed values of $A_{\perp}$ and $A_{||}$, eq 5 predicts $g_{\perp} = 1.916$ and $g_{\|} = 6.085$ (shown as green circles in Figure 12) compared with experimental values of $g_{\perp} = 1.924$ and $g_{\|} = 6.066$. Owing to the uncertainty of ±2% in the value $A_{\perp}$ derived from the simulation in Figure 2, the precision of this method is low, and we estimate $c_1^2 = 0.17 \pm 0.03$. The anomalous ^{171}Yb hyperfine interaction is therefore consistent with a configuration interaction coefficient similar to that obtained by other means.

Table 6. Experimental Spin Densities (%) on Ring Carbon Atoms

	C1	C2	C3	C4	C5	total
p-orbitals	−0.27	1.26	1.29	−0.29	2.26	4.25 ± 0.27
s-orbitals	−0.02	0.03	0.03	−0.02	0.06	0.07 ± 0.02
total	−0.29	1.28	1.32	−0.31	2.32	4.32 ± 0.30

4.5. Carbon-13 Hyperfine Coupling. Simulation of the HYSCORE spectra assumes perfect C_{3h} symmetry and one paramagnetic species and thus requires summing the hyperfine matrix contributions from the five carbon atoms from a Cp ring. The hyperfine matrix $\mathbf{A}^i$ for each Cp carbon atom i was modeled by point-dipolar contributions (T^{ij}_{dd}) due to spin density on Yb and the four adjacent carbons of the Cp ring, an isotropic contribution a^i_{iso} due to s-orbital spin density, and an axial contribution T^i_p due to π-orbital spin density.

$$\mathbf{A}^i_{total} = \sum_{j=1}^{5} \mathbf{T}^{ij}_{dd} + a^i_{iso}\mathbf{I} + \mathbf{T}^i_p$$

where bold symbols refer to matrices, italics to scalars, and $\mathbf{I}$ is the identity matrix. Each of the five point-dipolar matrices $\mathbf{T}^{ij}_{dd}$ are given (in Hz) by

$$\mathbf{T}^{ij}_{dd} = \rho_j \frac{\mu_0 g_e \beta_e g_n \beta_n}{2h} \frac{3\mathbf{n}_{ij}\mathbf{n}^T_{ij} - 1}{r^3_{ij}}$$

where $\mathbf{n}_{ij}$ and r_{ij} are respectively the unit column vector and the distance joining carbon i to the j^{th} point of spin density at Yb or one of the four adjacent Cp ring carbons. ρ_j is the total spin density associated with nucleus j. Contributions to the hyperfine coupling from spin density on adjacent Cp rings are negligibly small due to the $1/r^3$ dependence and their small spin density. Due to the large spin−orbit contribution from the Yb ion, this point-dipolar contribution was corrected with $\mathbf{T}^{so}_{dd} = \mathbf{T}_{dd} + \Delta\mathbf{g}\mathbf{T}_{dd}/g_e$, where $\Delta\mathbf{g} = \mathbf{g} - g_e\mathbf{I}$. The spin−orbit contribution for the spin density on the Cp ring is negligibly small.

The spin density in the ligand-centered a′ MO is not uniformly distributed (Figure 10b), being concentrated on C2, C3, and C5. Values obtained from a DFT calculation are listed in section S9 of the Supporting Information. While we have little confidence in their absolute magnitude, the distribution of spin density within each ring should be reliable, because it is primarily determined by the aromatic π-interactions. Thus, the DFT Cp carbon s- and π-orbital spin densities were used to provide a fixed set of scaling factors for the isotropic (n^i_s) and anisotropic (n^i_p) hyperfine coupling contributions for the carbon atoms, which are given by $a^i_{iso} = n^i_s A_s$ and $\mathbf{T}^i_p = n^i_p \mathbf{A}^i_p$. The coefficients n^i_s and n^i_p are shown in Table S9 of the Supporting Information. The matrices $\mathbf{T}^i_p$ have principal values $n^i_p(-A_p, -A_p, 2A_p)$, with the unique axes pointing perpendicular to the C′−C^i−C″ planes.

A_s and A_p are the only adjustable parameters and are used to match the simulated to the experimental HYSCORE spectra. The experimental s- and π-orbital spin densities for each carbon atom are calculated from the ratio of the experimental to the DFT hyperfine coupling multiplied by the corresponding DFT spin density, *e.g.* $\rho^i_{s,exp} = (a^i_{iso,exp}/a^i_{iso,DFT})\rho^i_{s,DFT}$ (cf. section S9 of the Supporting Information). The simulated spectra in Figure 3b use $A_s = 0.4 \pm 0.1$ MHz and $A_p = 1.6 \pm 0.1$ MHz. Table 6 lists the spin densities derived from these values.

Much weaker ridges in the spectra, corresponding to larger values of A_s and A_p, can be identified at lower contour levels (Figure S9.3 of the Supporting Information). We assign these to the minority species identified in the CW EPR spectrum (section 3.2.1); they have larger ^{13}C spin densities, so we speculate that they may contain one or more η_3-Cp rings. A ring orientation, in which an interacting allylic frontier MO has a nodal plane parallel to the nominal C_3 axis, would reduce the steric strain around the Yb atom, while concentrating an enhanced spin density on only two carbon atoms, as opposed to the more general distribution of the η_5 ring shown in Table 6.

The DFT calculation attributes a negative spin density of −2.3% to the five ring hydrogen atoms, and when scaled by the factor required to reproduce the experimental densities at carbon, this becomes −0.11% per ring. The net spin density associated with all three Cp ligands is then 12.6 ± 0.9%.

4.6. Visible/Near-IR Spectrum. *4.6.1. Introduction.* In 1967 Pappalardo and Jørgensen made a detailed spectroscopic study of thin sublimed films of $YbCp_3$ at nominal temperatures of 4.2, 77, and 298 K.[8] Noting a correlation between the energies of analogous broad transitions in four $LnCp_3$ compounds and their reduction potentials, they assigned the absorption near 16,000 cm^{-1} in $YbCp_3$ to a ligand-to-metal charge transfer excitation. In $TmCp_3$, for example, a similar transition is found at 23,800 cm^{-1}, consistent with a reduction potential for Tm^{3+} that is more negative by ∼1.2 eV. Although little further interpretation was possible in 1967, this data has proved to be invaluable.

Compared to conventional "ionic" Yb^{3+} compounds, the spectrum of $YbCp_3$ in the f−f region is highly anomalous, spanning an energy range that is an order of magnitude larger and between 20 to 50 times more intense. (Figure 4 and Table 3). We show in section 3.4 that almost all of the intensity between 9,000 and 20,000 cm^{-1} is vibronically "borrowed" from higher energy electric-dipole allowed transitions. The latter must be Cp → Yb charge-transfer excitations, because one-center excitations on Yb^{3+} (4f → 5d, at ∼5.5 eV)[56] and Cp^- ($\pi \rightarrow \pi^*$, at ∼5.6 eV)[57] are too high in energy to be significant.

In C_{3h} the a′ → a′ pure electronic transitions responsible for the visible absorption near 16,000 cm^{-1} are electric-dipole forbidden, whereas a″ → a′ and e′ → a′ charge transfer transitions, polarized respectively parallel and perpendicular to the principal axis, are allowed. We tentatively assign two broad and much more intense bands, with maxima at 23,530 and 26,060 cm^{-1}, to these allowed transitions (section 3.4.7). They are respectively 1.0 and 1.30 eV higher in energy than the a′ → a′ transitions—intervals that agree well with the 1.3 eV difference between the ionization energy of the a′ ligand MO and those attributed to the e′, e″, and a″ MOs (cf. Figure 10a).

4.6.2. Selection Rules and Intensities. In the C_{3h}* double group the electric-dipole operator transforms as $\Gamma_4(z)$ and $\Gamma_2,\Gamma_3(x \pm iy)$, and the allowed transitions are $\Gamma_7,\Gamma_8 \xrightarrow{z} \Gamma_9,\Gamma_{10}$ and $\Gamma_7,\Gamma_8 \xrightarrow{x\pm iy} \Gamma_9,\Gamma_{10} + \Gamma_{11},\Gamma_{12}$. In the model used to create Figure 11, the four excited states in the visible have the following symmetries: IV, Γ_7,Γ_8(forbidden); V, Γ_{11},Γ_{12} (allowed ⊥); VI, Γ_9,Γ_{10} (allowed ⊥ and ∥); VII, Γ_7,Γ_8 (forbidden). Their intensities support this assignment. The total vibronic intensity on origins IV and VII is ∼30−100 times more intense than that in the origin bands (Table 3), while origins V and VI have intensities that are similar in magnitude to that of the integrated vibronic structure built on them. Origin V at 11,385 cm^{-1} in the solution spectrum is particularly strong and sharp (cf. Figure 6).

Confirmation comes from the spectrum of the pyrrolidine adduct. The removal of the horizontal plane in the flattened tetrahedral geometry of this compound introduces a 10-fold increase in the intensity of the nominally forbidden transition to IV (section 3.4.5 and Table 4) and a 50% increase in the total band area based on the forbidden transition to origin VII, most of which is concentrated near the origin (section 3.4.6 and Table 4). There is however little intensity change in the region of origins V and VI, indicating that these pure electronic transitions are weakly electric-dipole allowed in the C_{3h} group. In $YbCp_3$ their intensity is unchanged in solution, while that in origin IV, attributable to the small out-of-plane displacement of Yb in the solid state, vanishes (Figure 5b) due to the presence of the C_{3h} plane.

The intensity of the $\Gamma_7,\Gamma_8 \overset{\perp}{\rightarrow} \Gamma_{11},\Gamma_{12}$ (V) transition is of particular interest. Although it is magnetic-dipole forbidden, the origin is strong ($f_{osc} \sim 2 \times 10^{-5}$) compared to a typical $^2F_{7/2} \rightarrow {}^2F_{5/2}$ transition ($f_{osc} \sim 1 \times 10^{-6}$) (Figure 4 and Tables 3 and 4), so its intensity must be attributed to CI. In the model of section 4.3.4, any CI is confined to the Γ_7,Γ_8 states (with orbital symmetry a′), while the basis of the Γ_{11},Γ_{12} states is pure 4f. It follows that the source of the intensity is an a′ → e′ orbital excitation (in the hole representation), with orbital transition moments of the form $\langle a'|e(x \pm iy)|4f_{\pm1}\rangle$. The dipole length in a two-center transition can be approximated by the distance of the (small) region of overlap density from the carbon nucleus, multiplied by the overlap integral S_{M-L}. From the $\langle r\rangle$ and $\langle 1/r\rangle$ for the Yb $4f_{5/2}$ and C (2p) orbitals,[58] we estimate that this region is centered ∼165 pm from the carbon nucleus. However, the ligand contribution to the ground state is such that the $c_1 = 0.35$, so that the effective dipole length is ∼58 pm. The experimental oscillator strength gives a dipole length of 0.75 pm, from which we estimate $S_{M-L} = 0.013$—a value that matches those in section 4.1.3.

This small overlap integral might appear incompatible with the relatively intense e′ → a′ transition in the 23,000 to 25,000 cm^{-1} region, in which the a′ hole, predominantly centered on the Yb atom, is filled from the e′ ligand MO. However, the latter orbital, while primarily composed of the same Cp(π) orbitals as the a′ ligand-centered MO, also contains substantial $5d_{\pm2}$ character, so that the transition moments contain a one-center term of the form $\langle 5d_{\pm2}|e(x \pm iy)|4f_{\pm3}\rangle$ that is intrinsically large. A closely related dipole length for the $f^{14}(^1S_0) \rightarrow f^{13}d(^1P_1)$ transition of Yb^{2+} ion was computed by Piper et al.,[56] using the wave functions of Herman and Skillman[59] and found to be 133 pm. The experimental intensity, section 3.4.7, gives a very approximate value for the dipole length in these transitions of ∼20 pm. Our DFT analysis (section S5 of the Supporting Information) gives the e′ ligand MO 5.8% 5d character, which, on the basis of Piper's calculation, would predict a dipole length of 32 pm, and is in fair agreement with the experimental value. There is thus a consistency between the assignment and characteristics of excited states VIII or IX and the theoretical description of the composition of the Cp-π bonding MOs.

On the basis of the theoretical orbital energies (section S5 of the Supporting Information), there should be an a″ → a′ charge transfer transition in the same spectral region as e′ → a′. However, S_{M-L} is too small for the two-center contributions to the transition moment to account for the experimental intensity, and we therefore look for one-center contributions. The only significant Yb contribution to the a″ orbital is $6p_z$ (4.3%), but the a′ hole has no Yb contributions other than $4f_{\pm3}$ (and to a much lesser extent $4f_{\pm2}$), so no intensity can attributed to this source. Consideration of the nodal structure of the ligand-centered parts of the a″ and a′ orbitals similarly indicates that they also cannot contribute to the intensity. The presence of a second intense transition at an energy of ∼3.0 V cannot therefore be readily assigned to this excitation. An alternative is suggested by the presence of a vacant orbital, with the composition of a 6s/$5d_0$ hybrid, 2.5 eV above the 4f shell, that is 1.2 eV more stable than any other virtual orbital.

The conclusion to be drawn from the above discussion is that among the intense transitions near 3 eV only the e′ → a′ charge transfer excitation, polarized perpendicular to the C_3 axis, is a plausible source of vibronic intensity in the near-infrared transitions.

4.6.3. Energies. The most striking feature of bands IV, V, and VI, nominally associated with the three components of the $^2F_{5/2}$ state of the Yb^{3+} ion, is that they span 1997 cm^{-1}. A survey of 24 different Yb^{3+} compounds (section S7 of the Supporting Information) shows that, on average, these components span 597 ± 185 cm^{-1}, with maximum and minimum values of 268 and 962 cm^{-1}. In the $YbCp_3$·pyrrolidine adduct, the span is also anomalously large at 1080 cm^{-1}, but roughly half that in pure $YbCp_3$.

These observations can be understood by reference to Figure 11. When $\delta_{CI} = 0$, the axial crystal field splits the $^2F_{5/2}$ state by 580 cm^{-1}, but when $\delta_{CI} = 3900$ cm^{-1}, the splitting between origins IV, V, VI, and VII increases sharply so that their energies approximately match those that are observed (green arrows in Figure 11). The shift in the energy of these transitions between the solution and solid phase implies that δ_{CI} is significantly larger in solution (Figure 5). For example, the separation between origins IV and V, VI increases by ∼80 cm^{-1}. An increase in δ_{CI} in the solution phase is consistent with the observations in section 4.3.4 concerning the solution phase *g*-values and the solid state magnetic moment.

As a result of the CI and the mixture of configurations in the ground state, some excitations, namely those to states V and VI, result in a net Yb → Cp charge-transfer, while those to states IV and VII involve a much larger transfer of charge in the opposite sense, i.e. Cp → Yb.

Donation from a pyrrolidine ligand raises the energy of the 4f shell relative to Cp(π), increasing the energy of the "charge-transfer" band near 16,000 cm^{-1} by ∼800 cm^{-1}. It also reduces the positive charge on the Yb atom, decreasing the 5d covalency and increasing the Yb−C bond length (experimentally by ∼5 pm; cf. section 3.3.1). Both factors reduce δ_{CI}, resulting in a decrease (Figure 11) in the splitting between bands IV, V, and VI, as observed.

These results can be compared with those from Amberger's group on tris(bis(trimethylsilyl)amido)ytterbium(III), or Yb-$(NSi_2)_3$.[60] These ligands are also strong donors, although the Si−N−Si planes are canted relative to the C_3 axis, to give an effective site symmetry of D_3 in solution, and the ligand field interaction differs from the $YbCp_3$ case due to the presence of nitrogen orbitals having π-symmetry with respect to the Yb−N bond. In the solid state there is disorder within the nominal D_3 site such that the Yb atoms lie above or below the plane of the amido groups by 52 pm to give a flattened trigonal pyramid local geometry, that is treated as having C_{3v} symmetry.[60,61]

In this case, the charge-transfer transition is found at 27,250 cm^{-1} (3.38 eV). The linearly polarized single crystal spectrum at 100 K shows three origins in the $^2F_{5/2}$ region, all of which are electric-dipole

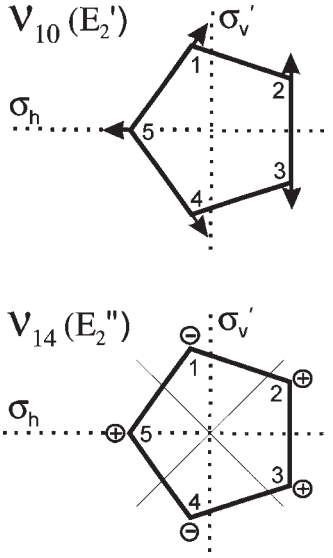

Figure 13. Selected internal modes of the Cp^- ion.

allowed and which together span 1380 cm^{-1}. Their polarizations confirm that the central band at 11,176 cm^{-1} has $\Gamma_{5,6}$ symmetry in C_{3v}*, which shares a basis with the C_{3h}* $\Gamma_{11,12}$ representation of origin V in $YbCp_3$. Within our model the increased charge-transfer energy in $Yb(NSi_2)_3$ would be expected to reduce substantially the contributions from the charge-transfer configuration, one feature of which is a reduced energy span of the states with $^2F_{5/2}$ parentage. Amberger et al.[60] employ an empirical Hamiltonian limited to the Ψ_0 $4f^{13}$ basis, so their parameters should not be compared to those obtained here.

4.6.4. Vibronic Structure. The prominent modes in the vibronic spectrum either are internal to the Cp ligand with $h\nu >$ 600 cm^{-1} or are associated with the $YbCp_3$ skeleton with $h\nu <$ 300 cm^{-1}.

Three normal modes of the Cp ligand at 1356, 1065, and 846 cm^{-1} are readily assigned to ν_{10}, ν_{11}, and ν_{12} (in the notation of Bencze[37]) and transform as E_2' in D_{5h}. The first of these, nominally a C−C stretching mode, is shown in Figure 13, in which σ_h represents the horizontal plane in $YbCp_3$ and σ_v' (not an operation of C_{3h}) represents a nodal plane in the molecular a′ orbital (cf. Figure 10). The ν_{11} and ν_{12} modes are nominally C−C−H and C−C−C in plane bends, but all three normal modes are mixtures of these primitive displacements.

In the charge-transfer configuration there is a distributed hole in the a′ MO. This orbital is bonding between C2−C3, and to a lesser extent between C5−C1 and C5−C4, and also antibonding between C1−C2 and C3−C4. Optical excitations that modify the extent of the CI should therefore excite ν_{10}, and to a lesser extent ν_{11} and ν_{12}. Comparable linear vibronic coupling occurs in the photoelectron spectrum of the Cp anion,[62] although this is complicated by a linear Jahn−Teller interaction along the same e_2' normal coordinate, due to the electronic degeneracy in the ground state of the Cp radical. This degeneracy is absent in the charge transfer configuration of $YbCp_3$ due to the large energy difference between the a′ and a″ Cp(π) MOs, but the linear electron−phonon coupling should be comparable. Lineberger et al. analyzed the photoelectron spectrum of $Cp^•$ and report theoretical coupling constants of 0.21, −0.11, and −0.06 eV for ν_{10}, ν_{11}, and ν_{12}, respectively,[62] which is consistent with the trend in the intensities of the sidebands in Figure 7c. The coupling constants for the C−H stretching modes are insignificant, and that for the a_1' symmetrical ring breathing mode is also small.[62] Consistent with these results, the latter modes do not appear in the optical spectrum of $YbCp_3$.

The 619 cm^{-1} ν_{14} out-of-plane bending mode, also a source of significant vibronic intensity, transforms as E_2'' in D_{5h}, and one of its components (Figure 13) folds the ring about the σ_v' electronic nodal plane. Charge transfer from the Cp(π) MO selectively removes electronic charge density from C2, C3, and C5, while leaving that on C1 and C4 almost unchanged. Given that a Yb atom with a net charge of ∼2+ is located over the center of the ring, the ν_{14} folding displacement is the expected response to the nonuniformity in the ring carbon charges arising from the charge transfer.

In $YbCp_3$ each of the four vibronically active local ring modes combine to give collective molecular modes of a′ and e′ symmetry. Only the latter provide a source of electric dipole intensity, which must be drawn from an allowed a′ → e′ electronic transition. The obvious source is one of the intense electric-dipole allowed transitions to states VIII or IX (section 3.4.7), which lie ∼1.0−1.3 eV to higher energy and which is readily mixed with the a′ states by the electron−phonon interaction, provided that an appropriate choice of phase is taken for the three constituent local ring displacements. The important point here is that the electron−phonon interaction responsible for this intensity is associated exclusively with the ligands orbitals, so that its presence is a direct indication of the extent of CI in the initial and final states of this group of "forbidden" electronic transitions.

Origins V and VI only exhibit weak vibronic structure attributable to internal ligand modes, while other origins, notably IV, show equally strong structure attributable to low frequency modes involving ring displacements relative to the Yb atom. The electric-dipole transition moment $\boldsymbol{\mu}$ for a vibronic transition from the ground state $|g\rangle$ to an electronic excited state $|i\rangle$ in which one quantum of a vibration with frequency ν is also excited is given by

$$\langle g|\boldsymbol{\mu}|i\rangle = \sum_k \frac{1}{\delta E_{gk}}\left(\frac{\hbar}{2\nu}\right)\langle g|\mathbf{q}|k\rangle\langle k|\boldsymbol{\mu}|i\rangle - \sum_k \frac{1}{\delta E_{ik}}\left(\frac{\hbar}{2\nu}\right)\langle g|\boldsymbol{\mu}|k\rangle\langle k|\mathbf{q}|i\rangle \quad (6)$$

where $\mathbf{q}$ is the electron−phonon coupling operator, $|k\rangle$ is an excited state that is electric dipole allowed from either $|g\rangle$ or $|i\rangle$, and δE_{gk} and δE_{ik} are the relevant energy differences. We now make two assumptions.

(a) There is only one significant state $|k\rangle$, namely that responsible for the intense absorption with energy δE_{gk} ∼ 3 eV. For states for which i = IV−VII, δE_{ik} is the range 1.75−1.00 eV. In section 4.6.2 we attributed the intensity near 3.0 eV to one-center transition moments of the form $\langle 5d_{\pm 2}|e(x \pm iy)|4f_{\pm 3}\rangle$, but analogous contributions of the type $\langle 5d_{\pm 2}|e(x \pm iy)|4f_{\pm 1}\rangle$ will ensure that the transition moments $\langle k|\boldsymbol{\mu}|i\rangle$ are also significant.

(b) States V and VI do not belong to the Γ_7,Γ_8 irreps whose states exhibit characteristics of CI, and they can therefore be attributed pure f^{13} character. The electron−phonon coupling of a typical lanthanide state is expected to be too small to account for the substantial vibronic oscillator

associated with these excited states, and we therefore write $\langle k|\mathbf{q}|i\rangle \approx 0$ when i = V or VI.

It follows that the vibronic intensity associated with origins V or VI originates in the first term in eq 6, is proportional to the square of the CI coefficient c_1 in the ground state, and is inversely proportional to $\delta E_{gk}{}^2$. By contrast, in the case of origin IV, both terms in eq 6 are significant. The first term is similar to that just discussed, but the second term now contains the electron−phonon coupling matrix element $\langle \mathrm{VIII}|\mathbf{q}|\mathrm{IV}\rangle$. If the coupling is effective only on the ligand centered component of IV, represented by the CI coefficient $c_1(\mathrm{IV})$, this coupling is expected, using the eigenvectors from the calculation in section 4.3.4, to be larger than that in the ground state by the factor $(c_1(\mathrm{IV})/c_1)(\delta E_{gk}/\delta E_{ik}) = 2.52$. The intensity derived in this way should therefore be six times more intense than that on origin V. In Table 4 the experimental ratio is 5.5 in the solid state and 8.0 in solution. This analysis can be extended to origin VII, whose vibronic transition moment relative to that on origin IV is given by $(c_1(\mathrm{VII})/c_1(\mathrm{IV}))(\delta E_{(\mathrm{VIII}-\mathrm{IV})}/\delta E_{(\mathrm{VIII}-\mathrm{VII})}) = 2.62$, so that the predicted ratio of the oscillator strengths in these two transitions is 6.9. The experimental ratio (Table 4) in solution is 6.2 (the value of 4.4 in the solid is less reliable due to the large baseline corrections that have been applied in band VII).

Three $YbCp_3$ skeletal modes, at 138, 211, and 267 cm^{-1}, are prominent on origin IV. We associated these with IR and Raman active modes at 112, 196, and 255 cm^{-1} (Table 2 and Table S2 of the Supporting Information), all of which have E′ symmetry, and are respectively a Cp−Yb−Cp in plane bend, an asymmetric combination of Yb−Cp tilting motions, and the asymmetric Yb−Cp stretch. It is easy to understand how the displacement relative to the Yb^{3+} ion in these modes might mix the electric-dipole forbidden a′ excited state, in which the ligand hole is uniformly distributed over all three rings, with the higher energy dipole-allowed e′ states, in which the hole amplitude is concentrated on either the x or y axes, in a configuration that would be modulated by the motion of the Yb^{3+} ion along either of these axes. The 138 cm^{-1} Cp−Yb−Cp bending mode appears to be the most strongly coupled of the three.

To summarize, the vibronic structure in the electronic spectrum is consistent with, and provides additional evidence for, the presence of the configuration interaction, as discussed above.

4.7. Configuration Interaction and Covalency. The energies, intensities, and vibronic structure in the electronic transitions all support the predictions of the CI model. In particular, the transition energies serve to constrain the values of the CI matrix element, $\delta_{\mathrm{CI}} = -3900 \pm 400$ cm^{-1} and the energy difference between the configurations as $\Delta E_{\mathrm{M-L}} = 6100 \pm 600$ cm^{-1}. The wide error limits in these quantities arise from a significant correlation between them.

The magnitude of δ_{CI} is conveniently discussed using the Superposition Model that has been used for the *ab initio* calculation of lanthanide CF parameters.[44,46] This is closely related to the Angular Overlap Model,[63−65] in that the influence of each ligand is treated as additive. The CF parameters are resolved into radial and angular contributions—a separation that allows the overall ligand field to be expressed in terms of the properties of one or more cylindrically symmetrical metal−ligand bonds. When applied to fluorides and oxides, the interactions include the ligand 2s, $2p_\sigma$, and $2p_\pi$ valence orbitals. Here, as a result of the bonding within the Cp ligand, we assume that the Yb−C overlap is confined to those C−2p atomic orbitals that constitute the Cp($2p-\pi$) MOs and is therefore comparable to the Yb−$2p_\sigma$ interaction in these much-studied "ionic" examples.

Table 7. Charge Transfer Energies and CI Coefficients

host	E(CT)/eV	c_1^2
CaF_2	8.61	0.002
$YbF_6{}^{3-}$	7.35	0.004
$LiScO_2$	6.02	0.005
$Y_3Al_5O_{12}$	5.79	0.005
Y_2O_3	5.46	0.006
$[LnCl_6]^{3-}$	4.55	0.008
$[LnBr_6]^{3-}$	3.63	0.012
$YbCp_3$	1.24	0.11

An *ab initio* calculation of the CF parameters arising from Pr−F and Pr−Cl bonds has been described by Newman.[46] The contributions to the CF interaction fall into two groups: (a) those associated with a pure 4f electron Slater-determinant, such as Ψ_0 in eq 1, and (b) those associated with covalency represented, as in the current case, by the contribution of the charge-transfer configuration Ψ_1.

The former group includes the classical electrostatic 4f electron ligand point-charge interaction while also allowing for the penetration of 4f charge into the distributed electronic charge on the ligand, as well as overlap and exchange contributions, associated with the orthogonalization of the 4f and ligand valence shells that arise from the Pauli exclusion between them.

The covalent component is determined by Ψ_1, weighted by the coefficient $c_1 = -N_{f\sigma}/D_{f\sigma}$. When c_1 is small, the denominator $D_{f\sigma}$ can be identified with the energy of the charge-transfer transition between the two configurations. The various contributions to $N_{f\sigma}$ are linearly dependent on the overlap integral $\langle 4f|\sigma\rangle$. In PrF_3, by far the largest of these is the interaction of the exchange-charge (i.e., the 4f−$2p(\sigma)$ overlap density) with the ligand nuclear and electronic charges.[46,47] Given that the overlap integral is small, it is perhaps surprising that in PrF_3, at a distance of 4.99 Bohr, $N_{f\sigma}$ is calculated to be 3273 cm^{-1} or 0.41 eV. However, integrals of similar magnitude have been calculated for the Sm^{2+}−F interaction in samarium doped BaFCl.[44] A recent and more sophisticated calculation for Yb^{3+} doped into Cs_2NaYF_6, which yields excellent agreement with the experimental ^{19}F hyperfine coupling constants, gives $N_{f\sigma} = 0.458$ eV (3700 cm^{-1}).[66] In the absence of appropriate computational tools, we now assume that $N_{f\sigma}$ is of comparable magnitude in $YbCp_3$, as is indeed suggested by the configuration interaction matrix element of 3900 cm^{-1} (0.48 eV) derived empirically in this work.

Values of $D_{f\sigma}$ can be deduced from the optical charge transfer energies for Yb^{3+} in various hosts and complexes[67,68] and are listed in Table 7, which also lists c_1^2 based on the obviously crude assumption that $N_{f\sigma}$ remains constant at 0.41 eV. In $YbCp_3$ the equivalent value of $D_{f\sigma}$, after taking into account the spin−orbit interaction in the $4f^{13}$ state, is 1.24 eV.

The conclusion to be drawn from Table 7 is that covalency, as measured by c_1^2, scales as the square of $1/E$(CT) and so plays only a minor part in determining the CF interactions in "ionic" compounds, but it rapidly becomes important when the orbital energies on the ligand approach those of the 4f shell in Yb^{3+}. There appears therefore to be nothing anomalous about the Yb−C overlap or the CI matrix element that depends on it. The significant covalent contribution in $YbCp_3$ is mainly determined

Table 8. Square of the CI Coefficient by Various Methods

observable	c_1^2
PES intensities	0.120
g-tensor principal values	0.124
^{171}Yb hyperfine coupling	0.17 ± 0.03
^{13}C hyperfine coupling	0.126 ± 0.009

by the very low energy of the ligand to metal charge-transfer transition, which is a consequence of the strong donor properties of the Cp^- ligand and the low reduction potential of Yb^{3+}.

5. CONCLUSION

This work seeks to quantify the extent of covalency in the 4f shell of Yb^{3+}, in terms of the contribution of the Cp → Yb^{3+} charge-transfer configuration in the ground state wave function. Table 8 summarizes values for the square of the configuration interaction (CI) coefficient c_1, obtained by four independent methods.

The two configurational components of the ground state give rise to distinct photoionization spectra at high photon energy, whose relative intensities allow a direct determination of c_1. The corollary of Cp → Yb charge-transfer is Yb → Cp spin transfer. The reduced spin-density on the ytterbium atom is revealed in the EPR experiment by a reduction in the ^{171}Yb hyperfine coupling, while the ^{13}C hyperfine interactions, as determined in the HYSCORE experiment, quantify the increase in spin density on the cyclopentadienyl carbon atoms. Each experiment provides a separate measure of c_1. Finally, the axial anisotropy in the *g*-tensor can also be used to determine this coefficient, because the axial component of the total angular momentum, nominally maintained by a very large spin−orbit interaction, can be effectively partially quenched through the participation of the charge-transfer configuration.

The highly anomalous energies, intensities, and vibronic structure in the electronic absorption spectrum also provide a strong indication of the presence of the charge-transfer configuration. Taken with the *g*-value anisotropy, the f−f excitation energies also constrain the magnitude of c_1.

From an analysis of the factors that control the CI coefficient, it appears that the absence of significant covalency in the 4f shell of conventional compounds should not be attributed to small overlap integrals, but rather to the large values of E_{CT} (Table 8) that are an inevitable consequence of the electropositivity of the lanthanides and the electronegativity of their common ligands.

For strongly donating electron-rich ligands, a substantial degree of 4f shell covalency is to be expected when the lanthanide(III) ions are readily reducible. For example, relative to Yb(III), the change in E_{CT}, averaged over a large number of III compounds, is −0.44, +0.72, and +1.23 eV for Eu, Sm, and Tm, respectively, but ∼+2 eV for Pr, Nd, Dy, Ho, and Er.[67] In this latter group, any 4f covalency in $LnCp_3$ compounds should therefore be small ($c_1^2 \leq 1.6\%$). It will, however, be of major significance in $EuCp_3$ and, though smaller than in $YbCp_3$, should also be easily identifiable in $SmCp_3$ and $TmCp_3$ ($c_1^2 \approx 3-4\%$). Clearly, a small increase in ligand basicity should greatly enhance this element of the covalency in ytterbium organometallics. Notice, however, that the proximity on the energy scale of a ligand frontier orbital that interacts strongly with the 4f shell, in our example $a'(f_{3c})$ (Figure 10a), is a consequence of the absence of its interaction with the 5d shell and arises from the C_{3h} symmetry. The generality of this type of covalency will therefore be limited, by the presence of 5d ligand orbital interactions, to cases where local symmetry constraints allow the ligand frontier orbital energies to approach those of the 4f shell.

Finally, we emphasize that our results only shed light on the characteristics of the 4f shell. They do not directly quantify bonding interactions in the 5d shell, and they should not be taken to imply that the bonding in lanthanide cyclopentadienyls is primarily "ionic".

■ ASSOCIATED CONTENT

Supporting Information. Crystallographic data (CIF) file, selected bond metric data, vibrational frequencies, EPR and HYSCORE data, a list of published Yb^{3+} EPR parameters, computational geometry optimizations, orbital energies and spin densities, and a list of published Yb^{3+} optical excitation energies, as well as a full list of authors for ref 28. This material is available free of charge via the Internet at http://pubs.acs.org.

■ AUTHOR INFORMATION

Corresponding Author
Bob.Denning@chem.ox.ac.uk

■ ACKNOWLEDGMENT

We thank Dr. Andrea Sella and Charlene Hunston of University College, London for providing samples of $YbCp_3$. The University of Oxford provided crystallographic services and a DTA studentship for M.I. The Engineering and Physical Sciences Research Council supported the Oxford Center for Advanced Electron Spin Resonance (Grant EP/D044855D/1) and also provided financial support for M.I.

■ REFERENCES

(1) Coreno, M.; de Simone, M.; Green, J. C.; Kaltsoyannis, N.; Narband, N.; Sella, A. *Chem. Phys. Lett.* **2006**, *432*, 17.
(2) Coreno, M.; de Simone, M.; Coates, R.; Denning, M. S.; Denning, R. G.; Green, J. C.; Hunston, C.; Kaltsoyannis, N.; Sella, A. *Organometallics* **2010**, *29*, 4752.
(3) Coates, R.; Coreno, M.; DeSimone, M.; Green, J. C.; Kaltsoyannis, N.; Kerridge, A.; Narband, N.; Sella, A. *Dalton Trans.* **2009**, 5943.
(4) Bond, A. M.; Deacon, G. B.; Newnham, R. H. *Organometallics* **1986**, *5*, 2312.
(5) Booth, C. H.; Walter, M. D.; Daniel, M.; Lukens, W. W.; Andersen, R. A. *Phys. Rev. Lett.* **2005**, 95.
(6) Booth, C. H.; Kazhdan, D.; Werkema, E. L.; Walter, M. D.; Lukens, W. W.; Bauer, E. D.; Hu, Y. J.; Maron, L.; Eisenstein, O.; Head-Gordon, M.; Andersen, R. A. *J. Am. Chem. Soc.* **2010**, *132*, 17537.
(7) Booth, C. H.; Walter, M. D.; Kazhdan, D.; Hu, Y. J.; Lukens, W. W.; Bauer, E. D.; Maron, L.; Eisenstein, O.; Andersen, R. A. *J. Am. Chem. Soc.* **2009**, *131*, 6480.
(8) Pappalardo, R.; Jørgensen, C. K. *J. Chem. Phys.* **1967**, *46*, 632.
(9) Schlesener, C. J.; Ellis, A. B. *Organometallics* **1983**, *2*, 529.
(10) Cosier, J.; Glazer, A. M. *J. Appl. Crystallogr.* **1986**, *19*, 105.
(11) Otwinowski, Z.; Minor, W. *Methods Enzymology*; Academic Press: New York, 1997.
(12) Sheldrick, G. M. *Acta Crystallogr., Sect. A* **2008**, *64*, 112.
(13) Sheldrick, G. M. Institut fur Anorganische Chemie der Universitat: Gottingen, Germany, 1998.
(14) Calle, C.; Sreekanth, A.; Fedin, M. V.; Forrer, J.; Garcia-Rubio, I.; Gromov, I. A.; Hinderberger, D.; Kasumaj, B.; Leger, P.; Mancosu, B.;

Mitrikas, G.; Santangelo, M. G.; Stoll, S.; Schweiger, A.; Tschaggelar, R.; Harmer, J. *Helv. Chim. Acta* **2006**, *89*, 2495.
(15) Schweiger, A.; Jeschke, G. *Principles of pulse electron paramagnetic resonance*; Oxford University Press: Oxford, U.K.; New York, 2001.
(16) Stoll, S.; Schweiger, A. *J. Magn. Reson.* **2006**, *178*, 42.
(17) ADF2004.01 ADF2010.02, S., *Theoretical Chemistry*; Vrije Universiteit: Amsterdam, The Netherlands, 2009; http://www.scm.com.
(18) te Velde, G.; Bickelhaupt, F. M.; Baerends, E. J.; Fonseca Guerra, C.; Van Gisbergen, S. J. A.; Snijders, J. G.; Ziegler, T. *J. Comput. Chem.* **2001**, *22*, 931.
(19) Fonseca Guerra, C.; Snijders, J. G.; te Velde, G.; Baerends, E. J. *Theor. Chem. Acc.* **1998**, *99*, 391.
(20) van Lenthe, E.; Baerends, E. J.; Snijders, J. G. *J. Chem. Phys.* **1993**, *99*, 4597.
(21) van Lenthe, E.; Baerends, E. J.; Snijders, J. G. *J. Chem. Phys.* **1994**, *101*, 9783.
(22) van Lenthe, E.; Snijders, J. G.; Baerends, E. J. *J. Chem. Phys.* **1996**, *105*, 6505.
(23) van Lenthe, E.; van Leeuwen, R.; Baerends, E. J.; Snijders, J. G. *Int. J. Quantum Chem.* **1996**, *57*, 281.
(24) Vosko, S. H.; Wilk, L.; Nusair, M. *Can. J. Phys.* **1980**, *58*, 1200.
(25) Becke, A. D. *Phys. Rev. A* **1988**, *38*, 3098.
(26) Becke, A. D. *J. Chem. Phys.* **1988**, *88*, 1053.
(27) Perdew, J. P. *Phys. Rev. B* **1986**, *33*, 8800.
(28) Frisch, M. J.; et al. *Gaussian 03*, rev. D.02; Wallingford, CT, 2004.
(29) Stephens, P. J.; Devlin, F. J.; Chabalowski, C. F.; Frisch, M. J. *J. Phys. Chem.* **1994**, *98*, 11623.
(30) Lee, C.; Yang, W.; Parr, R. G. *Phys. Rev. B* **1988**, *37*, 785.
(31) Becke, A. D. *J. Chem. Phys.* **1993**, *98*, 5648.
(32) Eggers, S. H.; Kopf, J.; Fischer, E. O. *Acta Crystallogr., Sect. C: Cryst. Struct. Commun.* **1987**, *43*, 2288.
(33) Baker, E. C.; Raymond, K. N. *Inorg. Chem.* **1977**, *16*, 2710.
(34) Deacon, G. B.; Fallon, G. D.; Forsyth, C. M.; Gatehouse, B. M.; Junk, P. C.; Philosof, A.; White, P. A. *J. Organomet. Chem.* **1998**, *565*, 201.
(35) Baisch, U.; Pagano, G.; Zeuner, M.; Barros, N.; Maron, L.; Schnick, W. *Chem.—Eur. J.* **2006**, *12*, 4785.
(36) Ni, C. H.; Deng, D. O.; Qian, C. T. *Inorg. Chim. Acta—F-Block Elem. Art. Lett.* **1985**, *110*, L7.
(37) Bencze, E.; Lokshin, B. V.; Mink, J.; Herrmann, W. A.; Kuhn, F. E. *J. Organomet. Chem.* **2001**, *627*, 55.
(38) Aleksanyan, V. T.; Borisov, G. K.; Devyatych, G. G.; Gachter, B. F.; Koningstein, J. A.; Schneider, B. E. *J. Raman Spectrosc.* **1974**, *2*, 345.
(39) Reinhard, C.; Gudel, H. U. *Inorg. Chem.* **2002**, *41*, 1048.
(40) Deloach, L. D.; Payne, S. A.; Chase, L. L.; Smith, L. K.; Kway, W. L.; Krupke, W. F. *IEEE J. Quantum Electron.* **1993**, *29*, 1179.
(41) Carnall, W. T.; Fields, P. R.; Wybourne, B. G. *J. Chem. Phys.* **1965**, *42*, 3797.
(42) Amberger, H. D.; Schultze, H. *Spectrochim. Acta, Part A: Mol. Biomol. Spectrosc.* **1987**, *43*, 1301.
(43) Angelov, B. M. *Chem. Phys. Lett.* **1975**, *31*, 503.
(44) Shen, Y. R.; Bray, K. L. *Phys. Rev. B* **1998**, *58*, 5305.
(45) Pearson, J. J.; Herrmann, G. F. *J. Appl. Phys.* **1969**, *40*, 1142.
(46) Newman, D. J. *Adv. Phys.* **1971**, *20*, 197.
(47) Newman, D. J.; Curtis, M. M. *J. Phys. Chem. Solids* **1969**, *30*, 2731.
(48) Hubbard, J.; Rimmer, D. E.; Hopgood, F. R. A. *Proc. Phys. Soc. London* **1966**, *88*, 13.
(49) Koster, G. F.; Dimmock, J. O.; Wheeler, R. G.; Schatz, H. *Properties of the Thirty-Two Point Groups*; MIT Press: Cambridge, MA, 1963.
(50) Wybourne, B. G. *J. Chem. Phys.* **1965**, *43*, 4506.
(51) Morrison, C. A.; Leavitt, R. P. *J. Chem. Phys.* **1979**, *71*, 2366.
(52) Zhou, X. J.; Reid, M. F.; Faucher, M. D.; Tanner, P. A. *J. Phys. Chem. B* **2006**, *110*, 14939.
(53) Freeman, A. J.; Desclaux, J. P. *J. Magn. Magn. Mater.* **1979**, *12*, 11.
(54) *Electron Paramagnetic Resonance*; Abragam, A., Bleaney, B., Eds.; Oxford: Clarendon Press: Oxford, 1970.
(55) Dong, H. N.; Wu, S. Y.; Luo, X. B.; Tang, H. *Spectrochim. Acta, Part A: Mol. Biomol. Spectrosc.* **2005**, *61*, 637.
(56) Piper, T. S.; Brown, J. P.; McClure, D. S. *J. Chem. Phys.* **1967**, *46*, 1353.
(57) Wagner, B. O.; Ebel, H. F. *Tetrahedron* **1970**, *26*, 5155.
(58) Desclaux, J. P. *At. Nucl. Struct. Tables* **1973**, *12*, 311.
(59) Herman, F.; Skillman, S. *Atomic Structure Calculations*; Prentice-Hall, Inc.: Englewood Cliffs, NJ, 1963.
(60) Amberger, H. D.; Jank, S.; Reddmann, H.; Apostolidis, C. *Z. Anorg. Allg. Chem.* **2007**, *633*, 398.
(61) Niemeyer, M. *Z. Anorg. Allg. Chem.* **2002**, *628*, 647.
(62) Lineberger, W. C.; Ichino, T.; Wren, S. W.; Vogelhuber, K. M.; Gianola, A. J.; Stanton, J. F. *J. Chem. Phys.* **2008**, *129*, 084310.
(63) Gerloch, M.; Woolley, R. G. *Prog. Inorg. Chem.* **1983**, *31*, 371.
(64) Schaffer, C. E.; Jørgensen, C. K. *Mol. Phys.* **1965**, *9*, 401.
(65) Newman, D. J.; Ng, B. *Rep. Prog. Phys.* **1989**, *52*, 699.
(66) Falin, M. L.; Anikeenok, O. A.; Latypov, V. A.; Khaidukov, N. M.; Callens, F.; Vrielinck, H.; Hoefstaetter, A. *Phys. Rev. B* **2009**, 80.
(67) Dorenbos, P. *J. Phys.: Condens. Matter* **2003**, *15*, 8417.
(68) Anikeenok, O. A.; Eremin, M. V.; Falin, M. L.; Konkin, A. L.; Meiklyar, V. P. *J. Phys. C: Solid State Phys.* **1984**, *17*, 2813.